Reactive transport modeling of coupled feldspar dissolution and secondary mineral precipitation and its implication for diagenetic interaction in sandstones

Guanghui Yuan*[1, 2] Yingchang Cao*[1, 2] Jon Gluyas[3] Zhenzhen Jia[1]

(1. School of Geosciences, China University of Petroleum, Qingdao, China 266580;

2. Laboratory for Marine Mineral Resources, Qingdao National Laboratory for Marine Science and Technology, Qingdao, 266071, China;

3. Department of Earth Sciences, Durham University, Durham, DH1 3LE UK)

Abstract: Dissolution of feldspars and precipitation of secondary minerals (kaolinite, illite and quartz) are significant diagenetic processes in arkosic sandstones. We examined moderately buried sandstones in the Eocene Shahejie Formation from two sags in the Bohai Bay Basin, East China. Three different types of mineral assemblages (MA) were identified: extensively leached feldspars with a large amount of authigenic kaolinite and quartz cement (MA-1), extensively leached feldspars with a large amount of authigenic kaolinite and minor quartz cement (MA-2), and extensively leached feldspars with a small amount of both authigenic kaolinite and quartz cement (MA-3).

Numerical simulations at the continuum scale using Geochemist's Workbench 9.0 were conducted to decipher the origin of the different mineral assemblages. The physicochemical reactions including feldspar dissolution, transport of Al^{3+} and SiO_2(aq), and precipitation of kaolinite and quartz are coupled together in these simulations, with constraints of chemical reactions, kinetic law, dispersion, and advection. Modeling results suggest that a dissolution zone, a transitional zone, and a precipitation zone can be formed in a sandstone unit with suitable constraints of temperature, flow rate, fluid composition and mineral reaction rate. And MA-3, MA-2, and MA-1 assemblages develop in these three zones respectively. The higher SiO_2(aq) concentration required for the saturation of quartz than for kaolinite and the low Al^{3+} concentration needed for the saturation of kaolinite lead to the precipitation of only kaolinite in the transitional zone in a geochemical system with feldspar dissolution serving as the dominant source of SiO_2(aq) and Al^{3+}.

Comparisons between modeling results and observations of natural sandstone diagenesis suggest that an MA-1 assemblage is likely to occur in buried sandstones at high temperatures (>70-80 °C) and low flow rates. An MA-2 assemblage may occur in moderately buried sandstones at moderate temperatures (40-70 °C), in deeply buried sandstones with faults and fractures serving as conduits of meteoric freshwater, or in shallow sandstones where meteoric water is not abundant. An MA-3 assemblage tends to occur in shallow sandstones at low temperatures (<40-50 °C) and high flow rates, or in buried sandstones where faults and fractures develop widely and serve as freshwater conduits. These proposals are valid in natural arkosic sandstones and of great significance in deciphering the diagenetic environments where the feldspar dissolution and secondary mineral precipitation have occurred.

Key words: Feldspar dissolution, mass transfer, kaolinite, quartz cement, sandstones, numerical modeling, Geochemist's Workbench 9.0

1 Introduction

Feldspar dissolution and precipitation of secondary minerals (quartz, kaolinite, and illite) are significant diagenetic reactions affecting the reservoir quality of subsurface sandstones with detrital feldspar grains (Bjørlykke and Jahren, 2012; Giles and De Boer, 1990; Glasmann, 1992; Ronald and Edward, 1990; Taylor et al., 2010; Wilkinson et al., 2014; Yuan et al., 2015a). Many petrographic studies have reported mineral assemblages of two end-members relating to feldspar leaching reactions (Giles and De Boer, 1990; Hayes and Boles, 1992; Taylor et al., 2010; Yuan et al., 2013). One end-member case is extensively leached feldspars coupled with a large amount of secondary pores, authigenic clays, and quartz cements in a closed system. The opposite end-member is extensively leached feldspars coupled with few secondary minerals but enhanced secondary pores in an open system. A third mineral assemblage related to feldspar diagenesis consists of extensively leached feldspars with massive authigenic kaolinite but minor quartz cement (Bjørlykke and Jahren, 2012; Emery et al., 1990; Yuan, 2015). The observed mineral and textural relationships, which indicate the significance of feldspar dissolution, are controlled by integrated physicochemical processes including feldspar dissolution, secondary mineral precipitation, and transfer of Al^{3+} and SiO_2(aq) in chemical weathering, diagenesis and hydrothermal alteration of sandstones (Barclay and Worden, 2000; Bjørlykke and Jahren, 2012; Farquhar et al., 2015; Fu et al., 2009; Giles and De Boer, 1990; Lu et al., 2013; Maher et al., 2009; Thyne et al., 2001; Yuan et al., 2015a).

Though numerous laboratory experiments on the kinetics of dissolution and precipitation of a range of feldspar compositions, kaolinite, and quartz under a wide range of chemical and physical conditions have been conducted (Fu et al., 2009; Ganor et al., 1995; Hangx and Spiers, 2009; Harouiya and Oelkers, 2004; Huang et al., 1986; Kampman et al., 2009; Maher et al., 2009; Yang and Steefel, 2008), only a few of these studies have considered mass transfer (eg. Al^{3+}, SiO_2(aq)). Most laboratory mineral dissolution experiments were performed in fluids far from equilibrium with minerals, though some experiments on mineral reactions close to equilibrium (Burch et al., 1993; Devidal et al., 1997; Gautier et al., 1994; Hellmann and Tisserand, 2006; Hellmann et al., 2010; Nagy et al., 1990; Yang and Steefel, 2008) and experiments on coupled feldspar dissolution and secondary mineral precipitation in batch systems with specific conditions were also reported recently (Burch et al., 1993; Fu et al., 2009; Hellmann and Tisserand, 2006; Hellmann et al., 2010; Lu et al., 2013; Zhu et al., 2010).

Reactive transport modeling is an essential and significant tool to investigate the water-rock interaction (Steefel et al., 2005; Thyne, 2001). Geochemical modeling studies for the purpose of understanding mineral dissolution, mass transfer, or coupled mass transfer and mineral dissolution/precipitation in different systems have been reported (Chen et al., 2014; Huber et al., 2014; Johnson et al., 1998; Kang et al., 2010; Maher et al., 2009; Park, 2014; Park and Ortoleva, 2003; Steefel et al., 2005; Steefel and Cappellen, 1990; Thyne, 2001; Thyne et al., 2001; Yuan et al., 2015b). Many studies have been conducted to investigate chemical weathering reaction processes at profiles in the earth surface environments using the reactive transport model (Maher et al., 2009; Navarre-Sitchler et al., 2011; Soler and Lasaga, 1996; Soler and Lasaga, 1998; Soler and Lasaga, 2000; Steefel and Cappellen, 1990). Numerical simulations of feldspar dissolution with precipitation of secondary minerals in subsurface sandstones have been conducted in many studies (Barclay and Worden, 2000; Xu et al., 2005; Yuan et al., 2015b), however, mass transfer was not included in most of the models that have been used. To date, only a few studies on coupled chemical reactions and mass transfer in feldspar dissolution processes in subsurface geochemical systems with specific conditions have been reported (Kampman et al., 2014; Maher et al., 2006; Park, 2014; Park and Ortoleva, 2003; Stoessell, 1987; Thyne, 2001; Thyne et al., 2001; White et al., 2005). Stoessell (1987)

studied the transport of Al^{3+} released from a single leached feldspar grain by diffusion coupled with advective flow in a two dimensional scheme at 100 °C (Stoessell, 1987). Thyne et al. (2001) and Thyne (2001) modeled transfer of K^+ and SiO_2(aq) by only diffusion and coupled feldspar dissolution and precipitation of illite and quartz in interbedded sandstones and mudstones in a one-dimensional scheme at 130°C (Thyne, 2001; Thyne et al., 2001). Maher et al (2006) investigated the apparent discrepancy between laboratory and field dissolution rates of plagioclase using various mechanistic reactive transport models (Maher et al., 2006). White et al. (2005) and Kampman et al. (2014) investigate the CO_2-fluid-mineral interactions during CO_2-injection in buried sediments (Kampman et al., 2014; White et al., 2005). Park (2014) introduced a method to simulate coupled mass-transfer and chemical reactions and reported a flow-through system where CO_2-charged water with a 100 m/yr flow rate interacted with formation water in sandstones at 90 °C in a one dimensional scheme (Park, 2014). Further studies using reactive transport modeling are necessary for a more thorough interpretation of the various diagenetic mineral assemblages associated with feldspar diagenesis in subsurface sandstones.

The Nanpu Sub-basin and the Dongying Sub-basin are two subunits in the Bohai Bay Basin and are important oil and gas producing provinces in East China (Guo et al., 2010; Guo et al., 2013). Detailed geological background knowledge is available from previous studies (Cao et al., 2014; Guo et al., 2010; Guo et al., 2013; Yuan et al., 2015a; Yuan et al., 2015b; Zhang et al., 2008). Based on studies of the sandstones in the Eocene Shahejie Formation in these two sags, three different types of mineral assemblages of leached feldspars, authigenic kaolinite and quartz cement were identified. The objectives of this paper are to (1) present typical mineral assemblages relevant to feldspar diagenesis in subsurface sandstones; (2) investigate the integrated processes of feldspar dissolution, transport of solutes released from leached feldspars and secondary mineral precipitation utilizing the Geochemist's Workbench 9.0 to address coupled mass-transfer and water-rock interactions at the continuum scale using reactive transport modeling; (3) analyze the impact of different controlling factors including temperature, flow rate and composition of CO_2-charged fluid, mineral reaction rate and fracture; and (4) propose favorable geological conditions for the occurrence of various mineral assemblages. This study show that reactive transport simulations can be used to decipher the occurrence of feldspar diagenesis in subsurface arkosic sandstones. The favorable geological conditions proposed for occurrence of the different diagenetic mineral assemblages is of great significance for understanding the diagenetic environments where the feldspar dissolution and secondary mineral precipitation have occurred and for prediction of reservoir quality of subsurface sandstones.

2 Samples and Methods

A petrography analysis on detrital mineral compositions and diagenetic chemical reactions in natural sandstone samples was conducted. Diagenetic mineral assemblage was identified using such analysis and the obtained petrography data can provide constraints for model formulation. Sandstone core samples from the Eocene Shahejie Formation in the Dongying Sub-basin and the Nanpu Sub-basin were used in this study. The samples were selected from different positions in the sandstone beds, consisting of medium grained sandstones to pebbly sandstones with little matrix.

Two hundred and fifty red (or blue) epoxy resin-impregnated thin sections were prepared for an examination of mineral compositions, secondary porosity in feldspars, and authigenic minerals. Oil in the core samples was removed first using alcohol-benzene compound. Impregnation was undertaken in a vacuum to remove gas from the samples; samples were dried at 50 °C and the Lvbao-E51 epoxy was cured at 60 °C and injected into the samples with a pressure of 50 Mpa. Then, samples were polished to be 30 μm

thick thin sections. Optical identification of the thin sections was conducted using a Zeiss (Axioplan 2 imaging) microscope. Point-counts were performed on the thin sections for the detrital compositions with at least 300 points, which can provide a standard deviation of approximately 6% (Van der Plas and Tobi, 1965). Between twenty and forty micrographs of thin sections were taken for each thin section to determine the content of secondary pores formed by the dissolution of feldspar compositions (feldspar-hosted pores), quartz cements and authigenic clays. Photomicrographs were obtained using 100× objectives, and covering an area of 6.45mm^2. Target minerals and pores in each micrograph were then identified under a microscope and were drawn on a computer screen using CorelDRAW. The total area of the target minerals and the pores in every micrograph was obtained using Image-Pro Plus software. Contents of these minerals and pores in each thin section were obtained by averaging the values obtained from all micrographs. Twenty micrographs were used for the medium-coarse grained sandstones, while 40 micrographs were used for the pebbly sandstones to minimize sampling bias. Generally, feldspar remnants accompany most feldspar-hosted pores. Moldic pore texture and oversized pore texture (larger than most grains) were used to identify the total dissolution of feldspar grains. Repetitive measurements of 10 samples illustrate that errors are generally less than 0.5%, 0.2% and 0.1% when test data range from 2-4%, 0.5-2% and 0-0.5%, respectively (Yuan et al., 2015a). Besides the thin sections, X-ray diffraction (XRD) analysis was conducted sandstone samples to collect the content of K-feldspars and plagioclases. A D8 Discover was used for XRD analysis with Cu-Ka radiation, a voltage of 40 kV, and a current of 25 mA. Prior to analysis, each ample was oven-dried at 40 °C for 2 days and ground to < 40 μm using an agate mortar to thoroughly disperse the rocks. No chemical pre-treatment was employed. Samples were scanned from 3 to 70 with a step size of 0.02.

Two 2-D simulated systems were formulated for this study. One represents a homogeneous sandstone system; the other represents a sandstone system with a fracture at its left side, enabling us to study its impact on water-rock interaction. Kinetic data for K-feldspar, albite, kaolinite and quartz, diffusion coefficient and dispersivity (α) of various solutes were collected from scientific publications (Alekseyev et al., 1997; Black et al., 2014; Boudreau, 1996; Harouiya and Oelkers, 2004; Kampman et al., 2009; Lasaga, 1984; Li and Gregory, 1974; Ovaysi and Piri, 2011; Palandri and Kharaka, 2004; Park, 2014; Steefel and Lasaga, 1994; Xu et al., 2005; Yang and Steefel, 2008). Equilibrium constants of different chemical reactions, numerical simulations of coupled feldspar dissolution, transfer of solutes (eg.Al^{3+}, SiO_2(aq)), and precipitation of kaolinite and quartz were studied using the Geochemist's Workbench 9.0 (GWB). The GWB Reaction Module accounts for chemical reactions with thermodynamic data in the thermo.dat file. The GWB Transport Module is a "time marching" program and accounts for the transport of chemical compositions by molecular diffusion, hydrodynamic dispersion, and advection. The domain's initial condition and the composition of a fluid that move into it were set first. The program predicts how the domain changes over time as it reacts with the migrating fluids in the following manner. The model discretizes the domain by dividing it into blocks and sets physical properties such as porosity and permeability for each block. A 25% core plug porosity was used as the initial porosity of the simulated sandstone systems. The core plug porosity was obtained from the studied Shahejie sandstones reported in previous studies (Yuan et al., 2015a), which has been analyzed using CMStm-300 core measurement system with N_2 and a confining pressure of 6 Mpa. The GWB program initializes the system through speciation calculations and a series of constraints. For each time step, the program calculates the water flow field and how transport affects the chemical composition of each block. The program then determines the chemical state of each nodal block corresponding to the revised composition and temperature, and reflecting the progress of any kinetic reactions.

3 Petrographic Observations in Feldspar-rich Sandstones

3.1 Sandstone detrital compositions

Medium grained sandstones to pebbly sandstones from the two sags consist mainly of lithic arkoses and feldspathic litharenites with large amount of detrital feldspars (Fig. 1). In sandstones of the Gaoliu area of the Nanpu Sub-basin (GL sandstones), the point-counting data indicates that the quartz volume content is 10-49% with an average of 27%, the feldspar content is 14-55% with an average of 36%, and the rock fragment content is 7-65% with an average of 37% (Fig. 1A1). Bulk rock XRD data indicates that K-feldspar mass content is 6-30% with an average of 11% and the plagioclase content is 13-32% with an average of 25% (Fig. 1A2-A3). In sandstones of the Shengtuo area (ST sandstones) and the Minfeng area (MF sandstones) of the Dongying Sub-basin, the quartz content is 5-63% with an average of 31%, the feldspar content is 4-74% with an average of 37 %, and the rock fragment content is 3-88% with an average of 30% (Fig. 1B1). Bulk rock XRD data indicates that K-feldspar content is 2-27% with an average of 11% and the plagioclase content is 2-46% with an average of 24% (Fig. 1B2-B3).

3.2 Mineral assemblages of leached feldspars and secondary minerals

Previous studies suggest a weak chemical dissolution in the subsurface sandstones in the Dongying Sub-basin and Nanpu Sub-basin, and mineral textures suggest an association of authigenic kaolinite and quartz cement with leached feldspars (including detrital feldspar grains and feldspar compositions in rock fragments) (Yuan et al., 2015a; Yuan et al., 2013; Yuan, 2015). Regarding the amount of leached feldspars and associated secondary minerals (kaolinite and quartz), three types of diagenetic mineral assemblages were identified in the ST, MF, and GL sandstones (Yuan et al., 2015a; Yuan, 2015).

(1) Mineral assemblage-1 (MA-1): Extensively leached feldspars with massive authigenic kaolinite and quartz cements (Fig. 2A1, A2)

In the ST sandstones, extensively leached feldspars are commonly accompanied by massive kaolinite and quartz cements in nearby primary pores. On a thin section scale, quantitative data from thin sections demonstrates positive relationships between the amount of feldspar porosity and that of secondary minerals (Fig. 3A1, A2).

(2) Mineral assemblage-2 (MA-2): Extensively leached feldspars with massive authigenic kaolinite and minor quartz cement (Fig. 2B)

Differing from the ST sandstones, extensively leached feldspars in the MF sandstones are commonly accompanied by massive amounts of kaolinite but minor quartz cement in nearby primary pores. On a thin section scale, quantitative data from thin sections demonstrates a positive correlation between the amount of feldspar porosity and that of kaolinite, while the amount of quartz cement is much smaller than the feldspar porosity (Fig. 3B1, B2).

(3) Mineral assemblage-3 (MA-3): Extensively leached feldspars with little authigenic kaolinite and quartz cement (Fig. 2C)

Contrasting with the ST sandstones, extensively leached feldspars in the GL sandstones are commonly accompanied by extremely small amounts of kaolinite and quartz cement. On a thin section scale, quantitative data from thin sections indicate that the amount of secondary minerals is much less than the feldspar porosity (Fig. 3 C1, C2).

4. Model Formulation and Input Constraints

4.1 Simulated systems

Two 2-D simulated systems including a homogeneous sandstone system and a sandstone system with a fracture at its left side were formulated. The 2-D homogeneous system is a 10m×2.1m sandstone bed; the long axis (10m) and wide axis (2.1m) are divided into 100 and 21 grids evenly, with the length of 10 cm for each block (Fig.4A). The 2-D sandstone system with a fracture parallel to the long axis at the left side is a 10m×2.01m bed. The long axis (10m) is divided into 100 grids evenly, with the length of 10 cm for each block; the wide axis (2.01m) is divided into 21 grids, the grid in the middle of the bed has a width of 1cm, and the other twenty grids have widths of 10 cm each (Fig. 4B). The fracture unit (five meters in length) is set in the middle of the left side of the system, and the width of the fracture is represented by the 1cm grid. Kaolinite and quartz were considered as secondary minerals associated with the dissolution of K-feldspar and albite. The physical parameters of the models were constrained by simplified compositions of the sandstones in the Bohai Bay Basin (Fig.1), and the composition of each unit in these two systems was set to be initially homogeneous within the sandstone unit. Each grid in the sandstone unit consists of 20% K-feldspar, 20% albite, 34% quartz, 1% kaolinite, and 25% porosity, while the grids in the fracture unit consist of no minerals but have 100% porosity.

Different temperatures (25 °C, 65 °C, and 100 °C), different flow rates (0.01 m/yr, 0.1 m/y, 1 m/yr, 10 m/yr, 100 m/yr, 1000 m/yr), and CO_2-charged fluids with different compositions (Table 1) were utilized to investigate the impact of these controlling factors on the transfer of Al^{3+} and SiO_2(aq) and the precipitation of kaolinite and quartz. The composition of the fluids is listed in Table 1. Initial pore water and inflowing fluid-1 with a low concentration of SiO_2(aq) and Al^{3+} were utilized for most simulations. In some simulations, inflowing fluids with various concentrations of Na^+, SiO_2(aq) and Al^{3+} were utilized in some simulations to study the impact of different ions on the water-rock interaction. As CO_2 exists commonly in subsurface sandstone reservoirs and can promote the feldspar leaching reactions, different pCO_2(g) (0.11 bar, 0.61 bar and 2.81 bar) were used in simulations with the three different temperatures (according to the equation of log pCO_2 = -1.45 + 0.019*T) (Smith and Ehrenberg, 1989).

4.2 Chemical reactions related to feldspar alternation

The dissolution of K-feldspar and albite) can be expressed by the following equations, provided that no precipitation of secondary minerals occurs (Giles and De Boer, 1990; Zhu and Lu, 2009):

$KAlSi_3O_8$ (K-feldspar) + 4 H^+ = 2 H_2O + K^+ + Al^{3+}+ 3SiO_2(aq) (1)

$NaAlSi_3O_8$ (albite) + 4 H^+ = 2 H_2O + Na^+ + Al^{3+}+ 3SiO_2(aq) (2)

Once concentrations of SiO_2(aq) and Al^{3+} exceed the concentrations needed for the saturation of secondary minerals (quartz, gibbsite, boehmite, kaolinite and illite), these minerals can precipitate, assuming that no kinetic barrier exists. Gibbsite and boehmite are generally formed at the very early stage (usually less than 1year) of feldspar dissolution experiments (Zhu and Lu, 2009). As the water-rock interaction in subsurface sandstones lasts for a very long time (millions of years), and gibbsite or boehmite were not identified in our studied sandstones and most other subsurface sandstones (Wilkinson et al., 2001), the precipitation of gibbsite and boehmite was not included in this study. Feldspars and kaolinite in sandstones react to form illite when temperature exceeds 125-130 °C (Chuhan et al., 2001; Franks and Zwingmann, 2010; Lander and Bonnell, 2010), and the occurrence of these complex reactions were beyond range of the interest of this study.

Precipitation of quartz and kaolinite minerals can be represented by:

SiO_2(aq) = Quartz (3)

$Al^{3+} + SiO_2(aq) + 2.5H_2O = 0.5Al_2Si_2O_5(OH)_4$ (kaolinite) $+3H^+$ (4)

Thus, the entire process of feldspar dissolution and precipitation of quartz and kaolinite can be represented by the following equations (Bauluz et al., 2008; Bjørlykke and Jahren, 2012; Giles and De Boer, 1990; Lanson et al., 2002):

$KAlSi_3O_8$ (K-feldspar) + (4-6m) $H^+ = mAl_2Si_2O_5(OH)_4$ (kaolinite) + $nSiO_2$(quartz) + K^+
+ (1-2m) Al^{3+}+(3-2m-n) SiO_2(aq) +(2-5m) H_2O (5)

$NaAlSi_3O_8$ (albite) + (4-6m) $H^+ = mAl_2Si_2O_5(OH)_4$ (kaolinite) + $nSiO_2$(quartz) + Na^+
+ (1-2m) Al^{3+}+ (3-2m-n) SiO_2(aq) +(2-5m) H_2O (6)

where m and n are constants.

Assume complete precipitation of $Al^{3+}$and SiO_2(aq), the coefficients for Al^{3+} and SiO_2(aq) on the right hand side of Eq. (5) and Eq. (6) are both zero, and the dissolution-precipitation processes are re-written as:

$KAlSi_3O_8$ (K-feldspar) + H^+ + $0.5H_2O$ = 0.5 $Al_2Si_2O_5(OH)_4$ (kaolinite) + 2 SiO_2(quartz) + K^+ (7)

$NaAlSi_3O_8$ (albite) + H^+ + $0.5H_2O$ = 0.5 $Al_2Si_2O_5(OH)_4$ (kaolinite) + 2 SiO_2(quartz) + Na^+ (8)

With suitable conditions, in-situ replacement of K-feldspars by albite occurs (Wilkinson et al., 2001), and this process can be represented by:

$KAlSi_3O_8$ (K-feldspar) + Na^+ = $NaAlSi_3O_8$(Albite) + K^+ (9)

4.3 Kinetic data used in simulations

For kinetically controlled mineral reactions, the most common way of modeling mineral dissolution and precipitation rates is using rate equations derived from transition state theory (TST) (Hellevang et al., 2013; Lasaga, 1984; Steefel and Lasaga, 1994; Xu et al., 2005):

$$r_m = k_m A_m a_{H^+}^n \left|\left[1 - \left(\frac{Q_m}{K_m}\right)^\mu\right]\right|^\nu = k_m A_m a_{H^+}^n \left|\left[1 - \exp\left(\frac{\Delta G_m}{RT}\right)^\mu\right]\right|^\nu \quad (10)$$

where m is the mineral index, r_m is the reaction rate (mol/s, positive values indicate dissolution and negative values precipitation), k_m is the rate constant (in mol/cm^{2}sec), A_m is the mineral's surface area (cm^2), a_{H^+} is the activity of H^+, and n is the empirical reaction order accounting for catalysis by H^+ in solution. Q_m and K_m are the activity product and the equilibrium constant for the chemical reactions, respectively. ΔG_m is Gibbs free energy of the reaction. R is the gas constant (8.31J/[mol.K]), and T is the absolute temperature (K). The parameters μ and υ are two empirical and dimensionless positive numbers.

If μ and υ are taken equal to unity, in a close to equilibrium region, the linear transition state theory rate law (L-TST) equation leads to rates that are orders of magnitude faster than the reaction rates obtained from experiments or natural sandstones where fluid-water system is close to equilibrium (Hellmann and Tisserand, 2006; Hellmann et al., 2010). A parallel rate law formulation (PRL) can better describe the mineral dissolution close-to-equilibrium (Hellmann and Tisserand, 2006; Hellmann et al., 2010; Maher et al., 2009). The vast majority of geochemical codes (including the GWB Reaction Module) used to model the water–rock interaction, however, employ kinetic rate laws that incorporate an f(ΔG) parameter based on the 'transition state theory' (TST) (Hellmann et al., 2010). Hallevang (2013) suggest that second-order non-linear functions derived from the TST with respect to chemical affinity (μ =1, υ=2) can be used to describe mineral reaction rates close-to-equilibrium (Hellevang et al., 2013). In the far-from-equilibrium region, the rate of this nonlinear function is similar to the data from the linear function, while in the near equilibrium region, this nonlinear function can generate a rate that is two to three orders of magnitude slower than the linear function, which should be much closer to the field rate. In this study, μ and υ were set to 1 and 2, respectively.

The most commonly used k_m values for K-feldspar, albite, quartz and kaolinite are those derived from laboratory experiments done at far-from-equilibrium conditions at approximately 25 °C (Palandri and

Kharaka, 2004). The temperature dependence of the reaction rate constant can be expressed reasonably well via the Arrhenius equation (Lasaga, 1984; Steefel and Lasaga, 1994), and it is convenient to approximate the rate constant dependency as a function of temperature (Xu et al., 2005):

$$k = k_{25} \exp\left[\frac{-\mathrm{Ea}}{\mathrm{R}}\left(\frac{1}{\mathrm{T}} - \frac{1}{298.15}\right)\right] \quad (11)$$

where Ea is the activation energy (KJ/mol), k_{25} is the rate constant at 25 °C (mol/cm^2/sec)， R is the gas constant, and T is the absolute temperature (K).

The parameters employed for the kinetic rate expression of K-feldspar, albite, kaolinite and quartz are listed in Table 2. The empirical reaction orders n with respect to H^+ in Eq. (10) are set to be 0.500, 0.457, 0.777, and 0 for K-feldspar, albite, kaolinite, and quartz with an acid mechanism, respectively (Palandri and Kharaka, 2004). The temperature-dependent kinetic rate constants are calculated from Eq. (11). The evolution of the surface area in natural geologic media is very complex (Steefel et al., 2015), especially for multi-mineralic systems, and is not quantitatively understood at present (Xu et al., 2005). For this study, the reactive surface areas of feldspars and quartz were taken from Sonnenthal and Spycher (2001), which were calculated assuming a cubic array of truncated spheres that make up the framework of the rock (Table 2) (Sonnenthal and Spyoher, 2001). Kaolinite has specific surface areas reaching up to approximately 10×10^4 cm^2/g (Yang and Steefel, 2008). Following compaction and cementation in sedimentary rocks, the valid grain surfaces will be reduced and only surfaces open to pores are potential areas for mineral reactions. In this study, the reactive surface areas of kaolinite in sandstones with 25% porosity were set at 25% of the values of incompact sediments (Table 2).

Dissolution of quartz and kaolinite is negligible in the studied sandstones (Cao et al., 2014; Yuan et al., 2015a; Yuan et al., 2015b) and most other subsurface sandstones with temperature lower than 120 °C (Glasmann, 1992; Hayes and Boles, 1992; Milliken, 2003). The GWB Reaction Module cannot resolve the mineral surface area for dissolution and precipitation separately. To avoid dissolution of quartz and kaolinite in the present simulations, the surface area of these two minerals was set to zero. In order to simulate the precipitation of both minerals, we used the GWB Reaction Module to set descriptions of nucleation for both minerals. Mineral crystal growth depends on the degree of supersaturation and temperature, and critical relative superstation is needed for mineral nucleation to occur (Li et al., 2003). With limited kinetic data on mineral nucleation and because quartz and kaolinite were present in the initial simulated system, the critical supersaturation needed for nucleation to occur was ignored in this study. With constraints of volumes and specific surface area of quartz and kaolinite, the surface areas for the precipitation of quartz and kaolinite were substituted with nucleus of 40cm^2/cm^3 and 600cm^2/cm^3 respectively in the sandstone units (Table 2), while in the fracture unit, the nuclei were set at 10 cm^2/cm^3 and 150 cm^2/cm^3 with an inverse proportion to the porosities in the two units.

4.4 Treatment of mass transport in simulated system

4.3.1 Hydrodynamic dispersion in porous sandstones

K^+, Al^{3+} and SiO_2(aq) released from leached feldspars are mobile within the porous sandstones (Park, 2014). Transport of these species in a porous medium by hydrodynamic dispersion includes two fundamental processes, namely, the molecular diffusion process and the mechanical dispersion process competing with or complementing diffusion (Ovaysi and Piri, 2011; Park, 2014).

The GWB Transport Module combines these two processes with a “Fickian” linear law. The hydrodynamic dispersive flux q_D (mol/cm^2/s) of a chemical component in solution can be given as:

$$q_D = -\varphi D_H \times \frac{dC}{dX} \quad (12)$$

where q_D is the dispersive flux, φ is the porosity, D_H is the coefficient of hydrodynamic dispersion, and C is the component's concentration.

The coefficient of hydrodynamic dispersion (D_H) is calculated as (Roychoudhury, 2001):

$$D_H = D_0 + \alpha v \quad (13)$$

where D_0 is the diffusion coefficient (cm^2/s), α is the dispersivity (cm), and v is the average fluid velocity (cm/s).

4.3.1.1 Diffusion in porous sandstones

Diffusion in a porous sediment system is slower than in an equivalent volume of water due to the convoluted path the solutes must follow to circumvent sediment particles (Boudreau, 1996). The mass transport of a component by diffusion in sedimentary rocks can be expressed by Fick's law:

$$M_t = -\varphi D_0 \times \theta^2 \times \frac{dC}{dX} \quad (14)$$

where M_t is the diffusion flux, D_0 is the diffusion coefficient of solutes in water (cm^2/s), C is the component's concentration, and θ^2 is the tortuosity factor of the sedimentary rock.

Tortuosity is generally a ratio of pore connectivity length to sediment sample length, thus its value is always greater than 1. In porous sedimentary rocks, the tortuosity of the flow path is determined by porosity, permeability and pore structure. Tortuosity can be expressed by Archie's equation (Archie, 1942) as:

$$\theta^2 = \varphi^{1-\eta} \quad (15)$$

where n is an adjustable exponent (Boudreau, 1996). The empirically fit value of η reported by Boudreau (1996) is 2.14 ± 0.03 and, with an average value of 2.14, the tortuosity of sandstone with 25% porosity is 4.86.

Diffusion of a solute is temperature dependent. Table 3 lists a compilation of individual diffusivities for some solutes as functions of temperature (Boudreau, 1996; Li and Gregory, 1974; Park, 2014). Except for H^+ and OH^-, the difference of diffusivities of the other solutes (K^+, $Al(OH)_3$, Al^{3+}, HCO_3^-, $SiO_2(aq)$) is generally less than one order of magnitude. As the GWB Transport Module cannot describe the diffusion coefficients of different solutes separately, diffusivities of $1\times10^{-5}cm^2/s$, $2\times10^{-5}cm^2/s$, and $3\times10^{-5}cm^2/s$ were utilized for these solutes in pure water at 25 °C, 65 °C, and 100 °C, respectively. In sandstone with 25% porosity, the effective diffusivities are approximately $2.0\times10^{-6}cm^2/s$, $4.1\times10^{-6}cm^2/s$, and $6.2\times10^{-6}cm^2/s$, respectively.

4.3.1.2 Mechanical dispersion in porous sandstones

Mechanical dispersion is the mechanical mixing of pore fluids resulting from local velocity fluctuations produced from the tortuous path followed by a pore fluid element moving through the pore network (Giles, 1987). The coefficient of mechanical dispersion coefficient can be given as:

$$D_m = \alpha v \quad (16)$$

where α is the dispersivity (cm), and v the average fluid velocity (cm/s).

The effect of mechanical dispersion increases with increasing water flow velocity. The relative significance of molecular diffusion and mechanical dispersion (D_H/D_0) in porous sedimentary rocks depends on the flow regime, which can be characterized by the non-dimensional Peclet number (Pe) (Bear, 1972):

$$P_e = \frac{lv}{D_0} \quad (17)$$

where l is a characteristic medium length scale and D_0 is diffusion coefficient of a solute. When Pe is less than one, molecular diffusion dominates, otherwise mechanical dispersion is more significant.

The characteristic pore length of a medium consisting of particles with diameter d and porosity φ is derived from (Roychoudhury, 2001):

$$l = \varphi \times \frac{d}{1-\varphi} \quad (18)$$

With a combination of equations 17 and 18, Pe in a medium consisting of particles with diameter d and porosity φ can be expressed by:

$$P_e = \varphi \frac{dv}{(1-\varphi)D_0} \quad (19)$$

With the relationship between D_H/D_0 and Pe (Ovaysi and Piri, 2011), D_H/D_0 can be obtained and α can be calculated utilizing Eq. (16). Table 4 lists a compilation of Pe, D_H/D_0, and α at different temperatures and flow rates in a sandstone with 25% porosity and average grain size of 0.05 mm. Because α_L (longitudinal dispersivity) and a_T (transverse dispersivity) are both needed in a 2-D transport simulation, the calculated values of α presented in Table 4 were used for α_L, and by default of GWB, a_T was set to be one-tenth of α_L.

4.3.2 Advective flow

The mass transport of a component by advective flow in porous rocks can be expressed by (Bjørlykke and Jahren, 2012):

$$q_A = qC \quad (20)$$

where q_A is the advective flux of the species, q is the specific discharge, and C is the component's concentration.

4.5 Other constraints

(1) Boundary conditions

In the present simulations, the unreacted inflowing fluid (Table 1) enters the system from the left side and the reacted fluid leaves the system at the right side. The bottom and top boundaries are no-flow boundaries. As fluid crosses the left boundary, it carries mass into the system by advection. Hydrodynamic dispersion and molecular diffusion may also add or remove mass from the system, in response to differences in compositions between the inflowing fluid and the fluid within the system. Where fluid exits the system, the fluid composition is fixed at the composition of fluid within the grids along the right boundary, and here chemical mass is advected from the system.

(2) Porosity evolution and permeability correlation

In both two simulated systems where minerals dissolve and precipitate, the program tracks the porosity evolution based on the net change in mineral volume.

The evolving porosity affects the calculated permeability and hence the flow rate and pattern within the system. The GWB Transport Module uses the following empirical correlation to calculate the permeability of the porous medium from the porosity and the mineral content:

$$\log K = A\varphi + B + \sum A_m X_m \quad (21)$$

where *K* is the permeability in darcy, φ is the porosity, A, B and A_m are empirical constants, and X_m is the volume fraction of a mineral indexed by m.

Clays have significant impact on sandstone permeability. In this study, the simulations modeled the physical and chemical occurrences for ten years, and only a small volume of kaolinite (generally < 0.5%) was generated (Fig. 6-9). This has little impact on permeability (Giles and De Boer, 1990). Thus, no mineral was considered for a correlation with the permeability. By default, the values for A and B in Eq.(17) were set to 15 and -5, respectively. The correlation, then, is

$$\log K = 15\varphi - 5 \quad (22)$$

which describes a trend that has been observed in sandstones. For simulations lasting for thousands to millions of years, however, the impact of secondary clay minerals on permeability should be considered.

(3) Flow rate

At any point of the simulation, the flow rate is given by Darcy's law

$$q = \frac{K\Delta h}{\mu L} \quad (23)$$

where q is the rate of discharge ($cm^3/cm^2/s$ or cm/s), K is the average permeability (darcys), μ is *the* viscosity (cp), Δh is the drop in hydraulic potential across the simulated system (atm), and L is the length of the simulated system (cm). As the permeability may change with position, the GWB Transport Module solves for q using a finite difference technique. The viscosity is estimated from the fluid's temperature and chlorinity.

(4) Length of time step

The dispersive transport is solved by the forward-in-time method in the GWB Transport Module, and the length of a time step (Δt) is limited by the von Neumann criterion

$$\left(\frac{2D_{xx}}{\Delta x^2} + \frac{2D_{yy}}{\Delta y^2}\right) \times \Delta t \leq 1 \quad (24)$$

where Δx is the grid spacing in the X-direction, Dxx is the dispersion in the X-direction, Δy is the grid spacing in the Y-direction, and Dyy is the dispersion in the Y-direction. If the marching procedure takes too long of a time step, the solution becomes numerically unstable. By this criterion, the maximum time step in a simulation decreases quadratically with the grid spacing.

Similarly, the Courant condition

$$\left(\frac{|v|}{\Delta x} + \frac{|v|}{\Delta y}\right) \times \Delta t \leq 1 \quad (25)$$

where v is the fluid velocity, must be honored when solving for the advective transport by the forward-in-time, upstream weighted method. By this criterion, fluid may move no farther in the system than the length of a grid block.

Since the GWB Transport Module solves for dispersion and advection at the same time, it figures the limiting value for a time step according to the combined von Neumann and Courant stability conditions, according to

$$\left(\frac{|v_x|}{\Delta x} + \frac{|v_y|}{\Delta y} + \frac{2D_{xx}}{\Delta x^2} + \frac{2D_{yy}}{\Delta y^2} + \frac{4D_{xy}}{\Delta x \Delta y}\right) \times \Delta t \leq 1 \quad (26)$$

The GWB evaluates this equation for Δt at each grid and uses the minimum value as the limiting time step.

5 Modeling Results

Tens of simulations were conducted for this study. The results suggested that the mineral saturation state, the concentration of SiO_2(aq) and Al^{3+}, and the mineral reaction rates reached a steady state after a specific time (commonly < 1-5 years) (Fig. 5). The simulation results for the tenth year are shown in the following figures (Fig. 5-15; Fig. A1-A12).

5.1 Mineral saturation and zonation of geochemical system

With suitable conditions, the homogeneous geochemical system can be divided into three zones from upstream to downstream as the dissolution zone (Zone-1), the transitional zone (Zone-2), and the precipitation zone (Zone-3), respectively, according to the saturation indices of the four minerals (Fig. 6A,

B). In the dissolution zone, the saturation indices of K-feldspar, albite, quartz, and kaolinite are less than 1; in the transitional zone, the saturation index of kaolinite is higher than 1, while the other three indices are less than 1; in the precipitation zone, the saturation indices of both quartz and kaolinite are higher than 1 while the values for K-feldspar and albite are still less than 1. Although pore water in the whole system is undersaturated with respect to feldspars, the feldspar saturation index increases from upstream to downstream (Fig. 8D, Fig. 9D). In the homogeneous system, the lengths of the three zones vary for the simulations with different constraints (Fig. 7-9). In the system with a fracture, the mineral saturation index in the fracture unit is generally much lower than that in the sandstone unit (Fig. 15 B4, B5; Fig. A12).

5.2 SiO_2(aq) and Al^{3+} in fluids

After ten years' reaction, the concentration of SiO_2(aq) is lower on the upstream (left) side of the system than on the downstream side (Fig. 7A, Fig. 8A, Fig. 9A), while the concentration of Al^{3+} exhibits opposite variation trends with the SiO_2(aq). The concentration of SiO_2(aq) in the system shows a negative correlation to the fluid flow rates (Fig. 7A, Fig. 8A, Fig. 9A), meanwhile, it took positive correlation between temperature (Fig. 11A), mineral reaction rate constant (Fig. 12A), and inflowing concentration of SiO_2(aq) (Fig. 13A). The concentrations of various solutes are lower in the fracture unit than in the sandstone unit (Fig. 15B2, B3; Fig. A12B).

5.3 Mineral reaction rates

At the tenth year, the feldspar dissolution rates exhibit a sharp decrease from the dissolution zone to the transitional zone and a gentle decrease from the transitional zone to the precipitation zone (Fig. 7E, Fig. 8E, Fig. 9E), with the increase of the saturation index (Fig. 7D, Fig. 8D, Fig. 9D) and pH (Fig. 7B, Fig. 8B, Fig. 9B) oriented from the upstream to the downstream side of the system (Alekseyev et al., 1997; Fu et al., 2009; Kampman et al., 2009; Zhu et al., 2010). In the dissolution zone, the precipitation rates of kaolinite and quartz are zero, while in the transitional and precipitation zones, the precipitation rates of these two minerals (Fig. 7H, Fig. 8H, Fig. 9H) evolve with the mineral saturation indices (Fig. 7G, Fig. 8G, Fig. 9G).

5.4 Reacted minerals and enhanced porosity

The Enhanced porosity is expressed as the volume difference between leached feldspars and precipitated secondary minerals (Giles and De Boer, 1990). After the reactions in the simulated system reach steady state, the amount of leached feldspars decreases sharply from the dissolution zone to the precipitation zone for each unit of time (Fig. 7F, Fig. 8F, Fig. 9F). In the dissolution zone, the feldspars are dissolved with no precipitation of secondary minerals (MA-3), and the enhanced porosity in the dissolution zone is equivalent to the volume of leached feldspars. In the transitional zone, feldspars are dissolved with the precipitation of kaolinite but no quartz. The amount of precipitated kaolinite increases as the saturation index increases, but is less than the amount calculated from reaction-7 and reaction-8 (MA-2). While in the precipitation zone, feldspars are dissolved with the precipitation of both kaolinite and quartz, and the amount of these secondary minerals may reach up to the amount calculated from reaction-7 and reaction-8 (MA-1) (Fig. 6C, Fig. 7I, Fig. 8I, Fig. 9I). In the transitional zone and the precipitation zone, the enhanced porosity is smaller than the volume of leached feldspars (Fig. 6D, Fig. 7C, Fig. 8C, Fig. 9C).

6 Discussion

6.1 Formation of transitional zone with kaolinite but no quartz

The MA-2 assemblage consisting of extensively leached feldspar with large amounts of authigenic kaolinite and minor authigenic quartz cement is common in natural sandstones (Bjørlykke and Jahren, 2012; Yuan, 2015). In numerical simulations, the transitional zone is also characterized by leaching of feldspars,

and precipitation of kaolinite but not of quartz (Fig. 6). Leached feldspars with large amounts of quartz cements and little kaolinite can rarely be identified in natural sandstones (Bjørlykke and Jahren, 2012; Hayes and Boles, 1992; Yuan et al., 2015a; Bauluz et al., 2008;) or in numerical simulations (Ketzer et al., 2009; Farquhar et al., 2014).

In order to interpret this phenomenon, the equilibrium constants of the leaching reactions of quartz and kaolinite (Fig. 10A) and the concentrations of SiO_2(aq) and Al^{3+} needed for the saturation of quartz and kaolinite (Fig. 10B) were calculated. The results show that the concentration of SiO_2(aq) needed for kaolinite saturation is general lower than that for quartz, particularly at high temperature, and the concentration of Al^{3+} needed for the kaolinite saturation is extremely low (Fig. 10). As temperature increases, the equilibrium constant of the quartz-leaching reaction increases, while the equilibrium constant of the kaolinite-leaching reaction decreases sharply. Consistent with these equilibrium constants, the concentration of SiO_2(aq) required for the quartz saturation increase as the temperature increases, but the concentrations of SiO_2(aq) and Al^{3+} needed for the kaolinite saturation decrease. These constraints indicate that in a geochemical system with feldspar dissolution as a dominate source of SiO_2(aq) and Al^{3+}, 1) a fluid (eg. point-D in Fig.10B) undersaturated with kaolinite probably is undersaturated with quartz, and this will lead to the formation of the dissolution zone; 2) a fluid (eg. point-P in Fig.10B) oversaturated with quartz will probably also be oversaturated with kaolinite, and this will lead to the formation of the precipitation zone; and 3) a fluid (eg. point-T in Fig.10B) undersaturated with quartz may be oversaturated with kaolinite, and this can lead to the formation of the transitional zone with precipitation of only kaolinite.

6.2 Controlling factors on distribution of three zones

6.2.1 Temperature and mineral reaction rate

A comparison of the simulation results with the same flow rate and inflowing fluid but different temperatures shows that the proportion of the dissolution zone in the simulated system tends to decrease as the temperature increases, while the precipitation zone tends to increase (Fig. 11).

The temperature affects the proportion of different zones in the simulated system by its impact on the mineral reaction rate constant (Giles, 1987; Thyne, 2001; Xu et al., 2005), the equilibrium constants of the chemical reactions, and the hydrodynamic dispersion. From 25 °C to 100 °C, the feldspar dissolution rate increases 50-200 times (Table 2), leading to a rapid release rate of SiO_2(aq) and Al^{3+} from the leached feldspars to the pore fluids in the geochemical system. From 25 °C to 100 °C, the concentration of SiO_2(aq) required for the saturation of quartz increases from 5 mg/L to 65 mg/L due to the increase of the equilibrium constant of reaction-3, and the concentration of SiO_2(aq) and Al^{3+} needed for the saturation of kaolinite decreases markedly from 8 mg/L to 1.5 mg/L and from 3.5 mg/L to 0.42 mg/L, respectively (Fig. 10B). The diffusion of a solute is temperature-dependent; however, Table 3 shows that the values of diffusivities of various solutes at 100 °C are less than four times the values at 25 °C. These variations induced by temperature indicate that the rate of increase in concentration needed for the saturation of quartz is much lower than the rate of increase in the releasing rate of the solutes from leached feldspars, which probably resulted in the changing proportion of different zones in the simulated systems.

Though a non-linear TST function was used to obtain mineral reaction rates close to the rates in natural sandstones, there is still uncertainty on the mineral rate constants. A comparison of the simulation results using the same temperature, inflowing fluid, and flow rate but different mineral reaction rate constants shows that the length of the dissolution zone in the simulated system tends to increase as the mineral reaction rate constant decreases, while the precipitation zone tends to decrease (Fig. 12). For example, if the mineral reactions occurred at the rate constants listed in Table 2, a flow rate of 10 m/yr would form a 0 m dissolution zone, a 0.3 m transitional zone and a 9.7 m precipitation zone. If the reaction rate constants

decrease by two orders of magnitude, a flow rate of 10 m/yr would form a 0.8 m dissolution zone, a 9.2 m transitional zone and a 0 m precipitation zone. This indicates that, if the mineral reaction rates in the field were slower than the rates used in the present study (Table 2), the possibility of MA-2 assemblage and MA-3 assemblage occurring in moderately-deeply buried sediments with high temperature and low flow rates will increase.

6.2.2 Inflowing fluid flow rate

The lengths of the dissolution zones and the transitional zones increase as the inflowing flow rates increase in simulations with the same temperature, inflowing fluid and reaction rate constant (Fig.7D, G; Fig.8D, G; Fig.9D, G), particularly for simulations with low temperatures or low reaction rate constants (Fig.7D, G).

The flow rate affects the proportion of the different zones in the simulated system through the advective transfer of dissolved solutes from upstream to downstream (Giles, 1987; Stoessell, 1987). For simulations with low flow rates (eg. <0.1m/yr at 65 °C) and when diffusion dominates the transfer of SiO_2(aq) and Al^{3+} (Giles, 1987; Ovaysi and Piri, 2011), a timely removal of these solutes from zones with extensively leached feldspars cannot occur, leading to in-situ precipitation of quartz and kaolinite and little enhanced secondary porosity in the whole simulated system (Fig.7-8, Fig.A3). For simulations with high flow rates (eg. 1000m/yr at 65 °C) and when advective flow dominates the transfer of SiO_2(aq) and Al^{3+} and allows the timely removal of these solutes from the whole system (Giles, 1987; Ovaysi and Piri, 2011), the precipitation of quartz and kaolinite is inconsequential and a significantly enhanced secondary porosity occurs, with the MA-3 assemblage formed in the simulated system.

6.2.3 Composition of inflowing fluid

The composition of inflowing fluids affects the proportion of different zones in the simulated system by its impact on saturation of different minerals. A comparison between simulations with different inflowing fluids demonstrates that if the inflowing fluid is saturated (or supersaturated) with quartz, no dissolution zone or transitional zone can be formed, even when the flow rate approach hundreds to thousands of meters per year (Fig. 13). This indicates that the occurrence of the MA-2 assemblage and the MA-3 assemblage probably arose in the presence of a large volume of meteoric freshwater flux.

The concentration of Na^+ or K^+ has a significant impact on the leaching reactions of albite and K-feldspar. An increase in the concentration of Na^+ (or K^+) tends to retard the dissolution of albite (or K-feldspar) (Fig. 14, Figure A11). This is consistent with the phenomena of a weak dissolution of albite (or K-feldspar) in sandstones with pore water containing a high concentration of sodium (or potassium) (Wilkinson et al., 2001). A high Na^+ concentration also affects the types of secondary minerals as potassium in K-feldspar can be directly replaced by sodium to form albite (Eq.9), and a smaller amount of kaolinite will be formed in such a case (Fig. 14H).

6.2.4 Fracture

A comparison between simulations in systems with and without a fracture demonstrates that the fracture can affect mass transfer and mineral precipitation in at least three manners (Fig. 15, Fig. A12). First, the existence of a fracture can accelerate the flow rate in the fracture unit (Fig. 15B1), leading to relative lower concentration of solutes and lower saturation state of all four minerals in the fracture unit than in the sandstone unit, and no kaolinite or quartz were formed in the fracture unit (Fig. 15A4-A5, B4-B5; Fig. A12 D, E); second, the fracture decelerates the flow rate of the fluid in sandstones along the fracture (Fig. 15B1, Fig. A12A), leading to a higher concentration of SiO_2(aq) and the formation of precipitation zones or a transitional zones in such sandstones (Fig. 15A4, B4); third, the fracture accelerates the flow rate of the fluid expelled from the end of fracture unit into the adjacent sandstone units (Fig.15B1), leading to a lower

concentration of SiO_2(aq) and lower saturation state of quartz and kaolinite in the adjacent sandstones (Fig.15B2, B3; Fig.A12A), and contributing to the formation of a dissolution zone or a transitional zone in the sandstones closing to the end of the fracture unit (Fig. 15B4, B5). Thus, with widely developed faults and fractures that serve as conduits of meteoric freshwater (Giles, 1987), the possibility that MA-2 and MA-3 assemblages occur in the subsurface sandstones will increase.

6.3 Comparison between modeling results and observations of natural diagenesis

Increased temperatures dramatically increase the mineral reaction rate constant (Table 2) and suggest that faster flow rates are needed to avoid precipitation of secondary minerals in the subsurface sandstones at higher temperatures, particularly for kaolinite. Figure 16 displays the maximum flow rates required for the precipitation of quartz and kaolinite in the whole sandstone system and the minimum flow rates required for avoiding the precipitation of secondary minerals in the whole sandstone system at different temperatures (depth), with reaction rate constants constrained by values in Table 2 and with a temperature gradient of approximately 3°C/100m (Yuan et al., 2015a; Guo et al., 2012; Bjørlykke, 2010). Rough groundwater flow rates in sedimentary rocks compiled by Giles (1987) show that flow rates in shallow unconfined aquifers with low temperature can reach up to thousands of meters per year, and the flow rates in confined aquifers were reported to range from 1 m to 30 m. When burial depth exceeds 2000 m, where the temperature is approximately 80 °C, the flow rates are probably lower than 1 m/yr without the existence of preferable conduits such as faults and fractures. Such flow rates at different depths (temperatures) were compiled in Figure 16 to compare with the flow rates required for the development of the dissolution zone with MA-1 assemblage, the transitional zone with MA-2 assemblage and the precipitation zone with MA-3 assemblage.

MA-1 assemblage (extensively leached feldspars with a large amount of authigenic kaolinite and quartz cements), according to Figure 16, probably occurs in sandstones with great depth (>1500 m), high temperature (> 70-80 °C) and low flow rate. Thin sections show that only the precipitation zone with MA-1 (Fig. 2A1, A2) was identified in these ST sandstones, while no dissolution zone with MA-3 and no transitional zone with MA-2 were formed. These physicochemical occurrences in the ST sandstone geochemical system are consistent with the results of simulations with high temperatures, high ion concentrations and low fluid flow rates (Fig. 9, Fig. 13, Fig. A7, Fig. A8). With constraints of petrography, fault systems, pore water chemistry, homogenization temperature of aqueous fluid inclusions in quartz overgrowths and $\delta^{18}O$ compositions of quartz overgrowths, the feldspar dissolution and the precipitation of quartz and kaolinite in the ST sandstones were also suggested to occur in a moderately-deeply buried 'closed' sandstone system with high water salinity, high temperatures ranging from 80 °C to 120 °C, and without an impact of meteoric freshwater. The flow rates of pore water in such a system were likely slower than 0.1-1 m/yr (Giles, 1987) as few fault was identified to connect such a system with regional unconformity or the earth's surface (Yuan et al., 2015a; Yuan, 2015).

MA-2 assemblage (extensively leached feldspars with large amount of authigenic kaolinite and minor quartz cement), according to Figure 16, may occur in subsurface sandstones at moderate temperature (40-70 °C), in shallow sandstones where meteoric freshwater is limited, or in deeply buried sandstones with some faults serving as freshwater conduits. Glasmann (1992) reported that feldspar dissolution was accompanied by the precipitation of massive kaolinite but minor quartz cement (MA-2) in Brent Group sandstones of the North Sea, with a burial depth from 1000 m to 2000 m and temperatures ranging from 40 to 80 °C (Glasmann, 1992). Similarly, in many other sandstones with large amounts of feldspars, homogeneous temperature of aqueous fluid inclusions in authigenic quartz suggested the precipitation of quartz cements when temperatures exceeded 80-90 °C (Guo et al., 2012; Higgs et al., 2007; Yuan et al.,

2015a; Yuan et al., 2013). However, isotopic data of authigenic kaolinite in these sandstones suggested that the precipitation of kaolinite started in a relatively shallow burial diagenetic stage with low temperatures (40-50 °C), and generally in the presence of meteoric water (Bird and Chivas, 1988; Bjørlykke and Jahren, 2012; Longstaffe and Ayalon, 1990).

MA-3 assemblage (extensively leached feldspars with small amount of authigenic kaolinite and quartz cement), according to Figure 16, probably occurs in shallow sandstones at low temperatures (<40-50 °C) and high flow rates (Giles, 1987) or in moderately-deeply buried sandstones where faults develop and meteoric freshwater is available (Yuan et al., 2015a; Yuan, 2015). Hayes and Boles (1992) reported a typical example of MA-3 assemblage (1-3% feldspar porosity with only 0.1%-0.2% kaolinite in thin sections) in meteoric-zone Vedder sandstones with temperature of 30-50 °C (Hayes and Boles, 1992), and suggested that the feldspars were dissolved by fresh meteoric water at shallower depth. These physicochemical occurrences in the Vedder sandstones are consistent with the results of simulations with low temperature, high flow rates, and low concentrations of SiO_2(aq) and Al^{3+} (Fig. A2).

Thin sections showed that the MA-3 assemblage (Fig. 2C) developed in most GL sandstone samples, the MA-2 developed in few sandstone samples, and the MA-1 could not be identified in the GL sandstones, these physicochemical occurrences in the GL sandstones are consistent with the results of simulations with high temperatures, low ion concentrations, high flow rates and fractures. With constraints of petrography, fault system, pore water chemistry, and homogenization temperature of aqueous fluid inclusions in quartz overgrowths, the feldspar dissolution and the precipitation of kaolinite and quartz were also suggested to occur in an open sandstone system with low water salinity, temperatures ranging mainly from 90 °C to 115 °C, and significant impact of meteoric freshwater. The flow rates of the pore water in such a system were likely to be greater than 10 m/yr (Giles, 1987), as widely developed faults were identified to connect such a system with regional unconformity and the earth's surface (Yuan et al., 2015).

6.4 Implication and significance

This work has shown that various assemblages of leached feldspars, authigenic kaolinite and quartz cements in subsurface sandstones can be explained by the influx of CO_2-charged fluids into geochemical systems with different temperatures, fluid flow rates, pore water chemistry and fractures. Comparisons between the modeling results with the field examples suggested that the favorable geological conditions proposed for occurrence of the different diagenetic mineral assemblages is of great significance for understanding the diagenetic environments where the feldspar dissolution and secondary mineral precipitation have occurred (Bjørlykke and Jahren, 2012; Chuhan et al., 2001; Giles, 1987; Yuan et al., 2015). Thus, identification of these minerals assemblages in subsurface sandstones can be easily employed to study the possible evolution of diagenetic environments in the subsurface sandstones.

With kinetic data and a simulated model close to that of a natural sandstone, this study indicates that accurate prediction of feldspar-hosted secondary pores and relevant chemical reactions in the subsurface sandstones is possible to be obtained using the reactive transport simulation, which can benefit the prediction of reservoir quality of subsurface feldspar-rich sandstones.

7 Conclusions

(1) Three types of diagenetic mineral assemblages relevant to feldspar diagenesis can be identified in subsurface sandstones: extensively leached feldspars with large amounts of authigenic kaolinite and quartz cements (MA-1), extensively leached feldspars with large amounts of authigenic kaolinite and few quartz cement (MA-2), and extensively leached feldspars with slight amounts of authigenic kaolinite and quartz cement (MA-3).

(2) Flow rates have a significant impact on the integrated feldspar dissolution - mass transfer - secondary mineral precipitation processes. Dominated by hydrodynamic transfer in a system with a low flow rate, SiO_2(aq) and Al^{3+} released from leached feldspars cannot be removed from the dissolution zone, leading to in-situ precipitation of kaolinite and quartz. However, in a system with moderately-high flow rate, these solutes can be removed in a timely manner, leading to the development of the dissolution zone and the transitional zone.

(3) Temperature affects the integrated feldspar dissolution - mass transfer - secondary mineral precipitation processes through its impact on the mineral reaction rates, the equilibrium constants of chemical reactions, and the hydrodynamic dispersion.

(4) The higher concentration of SiO_2(aq) needed for the saturation of quartz (than for kaolinite) and the extremely low concentration of Al^{3+} needed for kaolinite saturation lead to precipitation of kaolinite but not of quartz in the transitional zone.

(5) The MA-1 assemblage tends to occur in moderately-deeply buried sandstones with high temperatures, low flow rates, few faults and little impact of meteoric freshwater; the MA-2 assemblage tends to occur in sandstones with moderate temperatures or deeply buried sandstones with widely developed faults acting as conduits of meteoric freshwater; the MA-3 assemblage tends to occur in shallow sandstones with low temperatures and high flow rates or moderately-deeply buried sandstones with widely developed faults acting as conduits of meteoric freshwater.

Acknowledgments

This study was financially supported by the Natural Science Foundation of China Project (No. 41602138), a National Science and Technology Special Grant (No. 2016ZX05006-007), China Postdoctoral Science Foundation funded project (2015M580617), and Shandong Postdoctoral innovation project (201502028). We sincerely thank GCA associate editor Dr. Carl Steefel and another three anonymous reviewers for reviewing our work, they have provided great advices and constructive comments for different versions of this paper.

References:

Alekseyev, V.A., Medvedeva, L.S., Prisyagina, N.I., Meshalkin, S.S. and Balabin, A.I., 1997. Change in the dissolution rates of alkali feldspars as a result of secondary mineral precipitation and approach to equilibrium. Geochimica et Cosmochimica Acta, 61(6): 1125-1142.

Archie, G.E., 1942. The electrical resistivity log as an aid in determining some reservoir characteristics. Transactions of the AIME, 1(146): 54-62.

Barclay, S.A. and Worden, R.H., 2000. Geochemical modelling of diagenetic reactions in a sub-arkosic sandstone. Clay Minerals, 35(1): 57-67.

Bauluz, B., Mayayo, M.J., Yuste, A. and González López., J.M., 2008. Genesis of kaolinite from Albian sedimentary deposits of the Iberian Range (NE Spain): analysis by XRD, SEM and TEM. Clay Minerals, 43(3): 459-475.

Bear, J., 1972. Dynamics of fluids in porous media. New York. London and Amsterdam: American Elsevier.

Bird, M.I. and Chivas, A.R., 1988. Stable-isotope evidence for low-temperature kaolinitic weathering and post-formational hydrogen-isotope exchange in permian kaolinites. Chemical Geology, 72: 249-265.

Bjørlykke, K., 2010. Petroleum geoscience. Springer Heidelberg Dordrecht Lond, New York, 508 pp.
Bjørlykke, K. and Jahren, J., 2012. Open or closed geochemical systems during diagenesis in sedimentary basins: Constraints on mass transfer during diagenesis and the prediction of porosity in sandstone and carbonate reservoirs. AAPG Bulletin, 96(12): 2193-2214.
Black, J.R., Carroll, S.A. and Haese, R.R., 2014. Rates of mineral dissolution under CO_2 storage conditions. Chemical Geology, 399: 134-144.
Boudreau, B.P., 1996. The diffusive tortuosity of fine-grained unlithified sediments. Geochimica et Cosmochimica Acta, 60(16): 3139 - 3142.
Burch, T.E., Nagy, K.L. and Lasaga, A.C., 1993. Free energy dependence of albite dissolution kinetics at 80°C and pH 8.8. Chemical Geology, 105(1 – 3): 137-162.
Cao, Y.C. et al., 2014. Characteristics and origin of abnormally high porosity zones in buried Paleogene clastic reservoirs in the Shengtuo area, Dongying Sag, East China, pp. 346-362.
Chen, L., Kang, Q., Carey, B. and Tao, W., 2014. Pore-scale study of diffusion – reaction processes involving dissolution and precipitation using the lattice Boltzmann method. International Journal of Heat and Mass Transfer, 75: 483-496.
Chuhan, F.A., Bjørlykke, K. and Lowrey, C.J., 2001. Closed-system burial diagenesis in reservoir sandstones: Examples from the Garn Formation at Haltenbanken area, offshore mid-Norway. Journal of Sedimentary Research, 71(1): 15-26.
Devidal, J., Schott, J. and Dandurand, J., 1997. An experimental study of kaolinite dissolution and precipitation kinetics as a function of chemical affinity and solution composition at 150°C, 40 bars, and pH 2, 6.8, and 7.8. Geochimica et Cosmochimica Acta, 61(24): 5165-5186.
Emery, D., Myers, K.J. and Young, R., 1990. Ancient subaerial exposure and freshwater leaching in sandstones. Geology, 18(12): 1178-1181.
Farquhar, S.M. et al., 2015. A fresh approach to investigating CO_2 storage: Experimental CO_2 – water – rock interactions in a low-salinity reservoir system. Chemical Geology, 399: 98-122.
Franks, S.G. and Zwingmann, H., 2010. Origin and timing of late diagenetic illite in the Permian – Carboniferous Unayzah sandstone reservoirs of Saudi Arabia. AAPG Bulletin, 94(8): 1133-1159.
Folk, R. L., Andrews, P. B., and Lewis, D., 1970. Detrital sedimentary rock classification and nomenclature for use in New Zealand. New Zealand journal of geology and geophysics, 13(4), 937-968.
Fu, Q. et al., 2009. Coupled alkali-feldspar dissolution and secondary mineral precipitation in batch systems: 1. New experiments at 200 °C and 300 bars. Chemical Geology, 258(3-4): 125-135.
Ganor, J., Mogollón, J.L. and Lasaga, A.C., 1995. The effect of pH on kaolinite dissolution rates and on activation energy. Geochimica et Cosmochimica Acta, 59(6): 1037 - 1052.
Gautier, J.M., Oelkers, E.H. and Schott, J., 1994. Experimental study of K-feldspar dissolution rates as a function of chemical affinity at 150°C and pH 9. Geochimica Et Cosmochimica Acta, 58(21): 4549-4560.
Giles, M.R., 1987. Mass transfer and problems of secondary porosity creation in deeply buried hydrocarbon reservoirs. Marine and Petroleum Geology, 4(3): 188-204.
Giles, M.R. and De Boer, R.B., 1990. Origin and significance of redistributional secondary porosity. Marine and Petroleum Geology, 7(4): 378-397.
Glasmann, J.R., 1992. The fate of feldspar in Brent Group reservoirs, North Sea: A regional synthesis of diagenesis in shallow, intermediate, and deep burial environments. Geological Society, London, Special Publications, 61(1): 329-350.
Sonnenthal, E. and Spyoher, N., 2001. Drift-Scale Coupled Processes (DST and THC Seepage) Models. Office of Scientific & Technical Information Technical Reports.

Guo, X. et al., 2010. Oil generation as the dominant overpressure mechanism in the Cenozoic Dongying depression, Bohai Bay Basin, China. AAPG Bulletin, 94(12): 1859-1881.
Guo, X. et al., 2012. Petroleum generation and charge history of the northern Dongying Depression, Bohai Bay Basin, China: Insight from integrated fluid inclusion analysis and basin modelling. Marine and Petroleum Geology, 32(1): 21-35.
Guo, Y. et al., 2013. Hydrocarbon generation and migration in the Nanpu Sag, Bohai Bay Basin, eastern China: Insight from basin and petroleum system modeling. Journal of Asian Earth Sciences, 77: 140-150.
Hangx, S.J.T. and Spiers, C.J., 2009. Reaction of plagioclase feldspars with CO_2 under hydrothermal conditions. Chemical Geology, 265(1-2): 88-98.
Harouiya, N. and Oelkers, E.H., 2004. An experimental study of the effect of aqueous fluoride on quartz and alkali-feldspar dissolution rates. Chemical Geology, 205(1-2): 155-167.
Hayes, M.J. and Boles, J.R., 1992. Volumetric relations between dissolved plagioclase and kaolinite in sandstones: implications for aluminum msss transfer in the San Joaquin Basin, California. Origin, Diagenesis, and Petrophysics of Clay Minerals in Sandstone. SPEM Special Publication No.47: 111-123.
Hellevang, H., Pham, V.T.H. and Aagaard, P., 2013. Kinetic modelling of CO_2 – water – rock interactions. International Journal of Greenhouse Gas Control, 15: 3-15.
Hellmann, R. and Tisserand, D., 2006. Dissolution kinetics as a function of the Gibbs free energy of reaction: An experimental study based on albite feldspar. Geochimica et Cosmochimica Acta, 70(2): 364-383.
Hellmann, R., Daval, D. and Tisserand, D., 2010. The dependence of albite feldspar dissolution kinetics on fluid saturation state at acid and basic pH: Progress towards a universal relation. Comptes Rendus Geoscience, 342(7-8): 676-684.
Higgs, K.E., Zwingmann, H., Reyes, A.G. and Funnell, R.H., 2007. Diagenesis, Porosity Evolution, and Petroleum Emplacement in Tight Gas Reservoirs, Taranaki Basin, New Zealand. Journal of Sedimentary Research, 77(12): 1003-1025.
Huang, W.L., Bishop, A.M. and Brown, R.W., 1986. The effect of fluid/rock ratio on feldspar dissolution and illite formation under reservoir conditions. Clay Minerals, 21(4): 585-601.
Huber, C., Shafei, B. and Parmigiani, A., 2014. A new pore-scale model for linear and non-linear heterogeneous dissolution and precipitation. Geochimica et Cosmochimica Acta, 124: 109-130.
Johnson, J.W., Knauss, K.G., Glassley, W.E., Deloach, L.D. and Tompson, A.F.B., 1998. Reactive transport modeling of plug-flow reactor experiments: quartz and tuff dissolution at 240°C. Journal of Hydrology, 209(1 – 4): 81-111.
Kampman, N., Bickle, M., Becker, J., Assayag, N. and Chapman, H., 2009. Feldspar dissolution kinetics and Gibbs free energy dependence in a CO_2-enriched groundwater system, Green River, Utah. Earth and Planetary Science Letters, 284(3-4): 473-488.
Kampman, N., Bickle, M., Wigley, M. and Dubacq, B., 2014. Fluid flow and CO_2 – fluid – mineral interactions during CO_2-storage in sedimentary basins. Chemical Geology, 369: 22-50.
Kang, Q., Lichtner, P.C., Viswanathan, H.S. and Abdel-Fattah, A.I., 2010. Pore Scale Modeling of Reactive Transport Involved in Geologic CO_2 Sequestration. Transport in Porous Media, 82(1): 197-213.
Ketzer, J.M. et al., 2009. Water-rock-CO_2 interactions in saline aquifers aimed for carbon dioxide storage: experimental and numerical modeling studies of the Rio Bonito Formation (Permian), southern Brazil. Applied Geochemistry, 24: 760-767.
Lander, R.H. and Bonnell, L.M., 2010. A model for fibrous illite nucleation and growth in sandstones. AAPG Bulletin, 94(8): 1161-1187.
Lanson, B. et al., 2002. Authigenic kaolin and illitic minerals during burial diagenesis of sandstones: a review.

802 Clay Minerals, 37(1): 1-22.
803 Lasaga, A.C., 1984. Chemical kinetics of water‐rock interactions. Journal of Geophysical Research: Solid
804 Earth (1978–2012), 89(B6): 4009-4025.
805 Li, T.S., Livk, I. and Ilievski, D., 2003. Supersaturation and temperature dependency of gibbsite growth in
806 laminar and turbulent flows. Journal of Crystal Growth, 258(3-4): 409-419.
807 Li, Y.H. and Gregory, S., 1974. Diffusion of ions in sea water and in deep-sea sediments. Geochimica et
808 cosmochimica acta, 38(5): 703-714.
809 Longstaffe, F.J. and Ayalon, A., 1990. Hydrogen-isotope geochemistry of diagenetic clay minerals from
810 Cretaceous sandstones, Alberta, Canada: evidence for exchange. applied Geochemistry, 5: 657-668.
811 Lu, P. et al., 2013. Coupled alkali feldspar dissolution and secondary mineral precipitation in batch systems–2:
812 New experiments with supercritical CO 2 and implications for carbon sequestration. Applied Geochemistry, 30:
813 75-90.
814 Maher, K., Steefel, C.I., DePaolo, D.J. and Viani, B.E., 2006. The mineral dissolution rate conundrum: Insights
815 from reactive transport modeling of U isotopes and pore fluid chemistry in marine sediments. Geochimica et
816 Cosmochimica Acta, 70(2): 337-363.
817 Maher, K., Steefel, C.I., White, A.F. and Stonestrom, D.A., 2009. The role of reaction affinity and secondary
818 minerals in regulating chemical weathering rates at the Santa Cruz Soil Chronosequence, California. Geochimica
819 et Cosmochimica Acta, 73(10): 2804-2831.
820 Milliken, K.L., 2003. Late diagenesis and mass transfer in sandstone shale sequences. Treatise on geochemistry,
821 7: 159-190.
822 Nagy, K.L., Steefel, C.I., Blum, A.E. and Lasaga, A.C., 1990. Dissolution and precipitation kinetics of kaolinite:
823 Initial results at 80°C with application to porosity evolution in a sandstone. AAPG Memoir, AAPG, Tulsa, OK:
824 85-101.
825 Navarre-Sitchler, A., Steefel, C.I., Sak, P.B. and Brantley, S.L., 2011. A reactive-transport model for weathering
826 rind formation on basalt. Geochimica et Cosmochimica Acta, 75(23): 7644-7667.
827 Ovaysi, S. and Piri, M., 2011. Pore-scale modeling of dispersion in disordered porous media. Journal of
828 Contaminant Hydrology, 124(1-4): 68-81.
829 Palandri, J.L. and Kharaka, Y.K., 2004. A Compilation of Rate Parameters of Water-Mineral Interaction
830 Kinetics for Application to Geochemical Modeling. No. OPEN-FILE-2004-1068. Geological Survey Menlo Park
831 Ca, 2004.
832 Park, A.J., 2014. Water-rock interaction and reactive-transport modeling using elemental mass-balance approach:
833 I. The methodology. American Journal of Science, 314(3): 785-804.
834 Park, A.J. and Ortoleva, P.J., 2003. WRIS. TEQ: multi-mineralic water‐rock interaction, mass-transfer and
835 textural dynamics simulator. Computers & geosciences, 29(3): 277-290.
836 Ronald, K.S. and Edward, D.P., 1990. Secondary porosity revisited: The chemistry of feldspar dissolution by
837 carboxylic. Acids and Anions AAPG, 74: 1795-1808.
838 Roychoudhury, A.N., 2001. Dispersion in Unconsolidated Aquatic Sediments. Estuarine, Coastal and Shelf
839 Science, 53(5): 745-757.
840 Smith, J.T. and Ehrenberg, S.N., 1989. Correlation of carbon dioxide abundance with temperature in clastic
841 hydrocarbon reservoirs: relationship to inorganic chemical equilibrium. Marine and Petroleum Geology, 6(2):
842 129-135.
843 Soler, J.M. and Lasaga, A.C., 1996. A mass transfer model of bauxite formation. Geochimica Et Cosmochimica
844 Acta, 60(60): 4913-4931.
845 Soler, J.M. and Lasaga, A.C., 1998. An advection–dispersion–reaction model of bauxite formation. Journal of

Hydrology, 209(1−4): 311-330.
Soler, J.M. and Lasaga, A.C., 2000. The Los Pijiguaos bauxite deposit (Venezuela): A compilation of field data and implications for the bauxitization process. Journal of South American Earth Sciences, 13(1−2): 47-65.
Steefel, C., Depaolo, D. and Lichtner, P., 2005. Reactive transport modeling: An essential tool and a new research approach for the Earth sciences. Earth and Planetary Science Letters, 240(3-4): 539-558.
Steefel, C.I. and Cappellen, P.V., 1990. A new kinetic approach to modeling water-rock interaction: The role of nucleation, precursors, and Ostwald ripening. Geochimica Et Cosmochimica Acta, 54(10): 2657-2677.
Steefel, C.I. and Lasaga, A.C., 1994. A coupled model for transport of multiple chemical species and kinetic precipitation/dissolution reactions with application to reactive flow in single phase hydrothermal systems. American Journal of Science, 294(5): 529-592.
Steefel, C.I., Beckingham, L.E. and Landrot, G., 2015. Micro-Continuum Approaches for Modeling Pore-Scale Geochemical Processes. Reviews in Mineralogy & Geochemistry, 80(1): 217-246.
Stoessell, R.K., 1987. Mass transport in sandstones around dissolving plagioclase grains. Geology, 15(4): 295-298.
Taylor, T.R. et al., 2010. Sandstone diagenesis and reservoir quality prediction: Models, myths, and reality. AAPG Bulletin, 94(8): 1093-1132.
Thyne, G., 2001. A model for diagenetic mass transfer between adjacent sandstone and shale. Marine and Petroleum Geology, 18(6): 743-755.
Thyne, G., Boudreau, B.P., Ramm, M. and Midtbo, R.E., 2001. Simulation of potassium feldspar dissolution and illitization in the Statfjord Formation, North Sea. AAPG bulletin, 85(4): 621-637.
Van der Plas, L. and Tobi, A.C., 1965. A chart for judging the reliability of point counting results. American Journal of Science, 263(1): 87-90.
White, S.P. et al., 2005. Simulation of reactive transport of injected CO_2 on the Colorado Plateau, Utah, USA. Chemical Geology, 217(3-4): 387-405.
Wilkinson, M., Haszeldine, R.S., Morton, A. and Fallick, A.E., 2014. Deep burial dissolution of K-feldspars in a fluvial sandstone, Pentland Formation, UK Central North Sea. Journal of the Geological Society, 171(5): 635-647.
Wilkinson, M., Milliken, K.L. and Haszeldine, R.S., 2001. Systematic destruction of K-feldspar in deeply buried rift and passive margin sandstones. Journal of the Geological Society, 158(4): 675-683.
Xu, T., Apps, J.A. and Pruess, K., 2005. Mineral sequestration of carbon dioxide in a sandstone − shale system. Chemical Geology, 217(3-4): 295-318.
Yang, L. and Steefel, C.I., 2008. Kaolinite dissolution and precipitation kinetics at 22°C and pH 4. Geochimica et Cosmochimica Acta, 72(1): 99-116.
Yuan, G. et al., 2015a. Feldspar dissolution, authigenic clays, and quartz cements in open and closed sandstone geochemical systems during diagenesis: Typical examples from two sags in Bohai Bay Basin, East China. AAPG Bulletin, 99(11): 2121-2154.
Yuan, G. et al., 2015b. Selective dissolution of feldspars in the presence of carbonates: The way to generate secondary pores in buried sandstones by organic CO_2. Marine and Petroleum Geology, 60: 105-119.
Yuan, G.H. et al., 2013. Feldspar dissolution and its impact on physical properties of Paleogene clastic reservoirs in the northern slope zone of the Dongying sag. Acta Petrolei Sinica, 34(5): 853-866. (In Chinese with English abstract).
Yuan, G.H., 2015. Genitic mechanism of dissolution of feldspars and carbonate minerals during diagenesis and its impact on reservoir poroperm (In Chinese with English abstract): Ph.D. thesis, China University of Petroleum (East China), Qingdao, China, 166 pp.

Zhang, W.C., Li, H., Li, H.J., Meng, Y.L. and Yang, F.B., 2008. Genesis and distribution of secondary porosity in the deep horizon of Gaoliu area, Nanpu Sag. Petroleum Exploration and Development, 35(3): 308-312.

Zhu, C. and Lu, P., 2009. Alkali feldspar dissolution and secondary mineral precipitation in batch systems: 3. Saturation states of product minerals and reaction paths. Geochimica et Cosmochimica Acta, 73(11): 3171-3200.

Zhu, C., Lu, P., Zheng, Z. and Ganor, J., 2010. Coupled alkali feldspar dissolution and secondary mineral precipitation in batch systems: 4. Numerical modeling of kinetic reaction paths. Geochimica et Cosmochimica Acta, 74(14): 3963-3983.

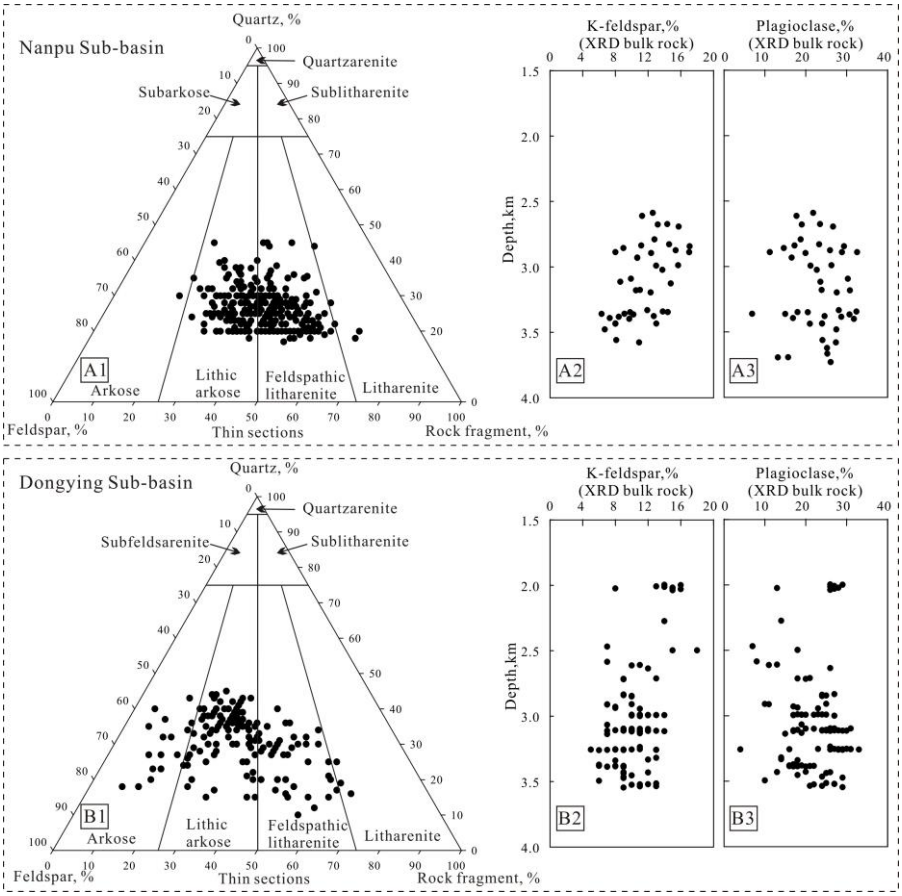

Figure 1. Ternary plots showing grain compositions of the GL sandstones (A1) in the Nanpu Sub-basin and the ST and MF sandstones (B1) in the Dongying Sub-basin (Refer to sandstone classification standard of Folk et al. 1970); A2-A3: the content of K-feldspar and plagioclase in the GL sandstones; B2-B3: the content of K-feldspar and plagioclase in the ST sandstones and the MF sandstones (Yuan et al., 2015a).

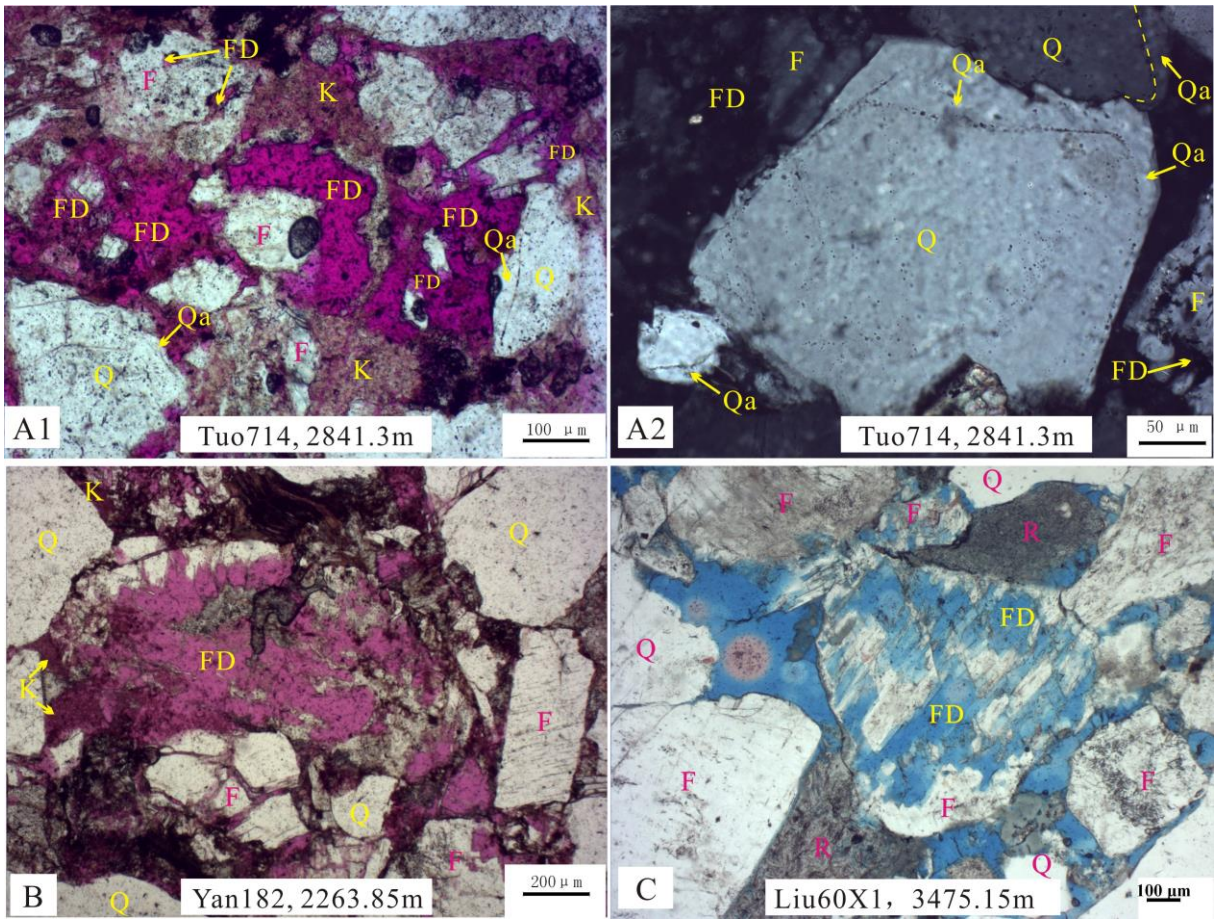

Figure 2. Micropetrographic evidences of the three types of mineral assemblages of leached feldspars, authigenic kaolinite and quartz cement in the Eocene Shahejie sandstones from two different sub-basins of the Bohai Bay Basin. A1-A2: Extensively leached feldspars with large amount of authigenic kaolinite and quartz, thin section at 2841.3m of well Tuo714 in the Shengtuo area of the Dongying Sub-basin; B: Extensively leached feldspars with large amount of authigenic kaolinite and minor quartz cement, thin section at 2263.85m of well Yan182 in the Minfeng area of the Dongying Sub-basin; C: Extensively leached feldspars with a very small amount of authigenic kaolinite and quartz cements, thin section at 3475.15m of well Liu60X1 in the Gaoliu area of the Nanpu Sub-basin. FD-secondary pores formed by feldspar dissolution, Qa-quartz overgrowth; K-kaolinite, Q-quartz, F-feldspar, R-aluminosilicate rock fragment.

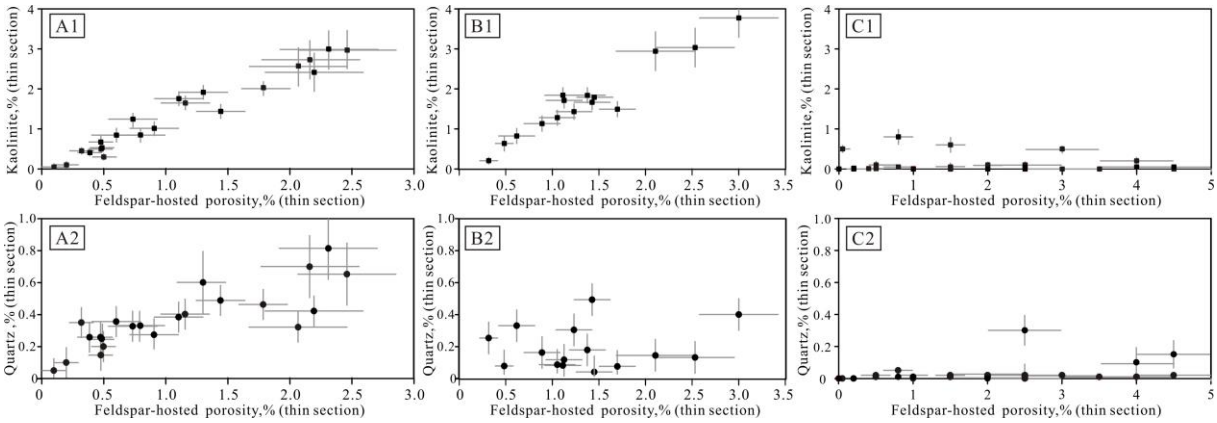

Figure 3. Plots illustrating the amount of feldspar-hosted porosity versus the amount of secondary minerals in the ST sandstones with MA-1 (A1, A2), the MF sandstones with MA-2, and the GL sandstones with MA-3 (C1, C2).

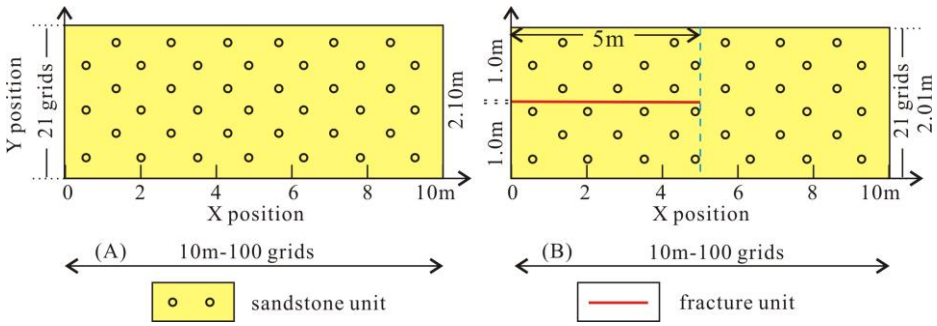

Figure 4. Schematic representation of two 2-D modelling systems, advection fluid flows from the left side to the right side. A: homogeneous sandstone system; B: heterogeneous sandstone system with a fracture parallel to the long axis at the left side.

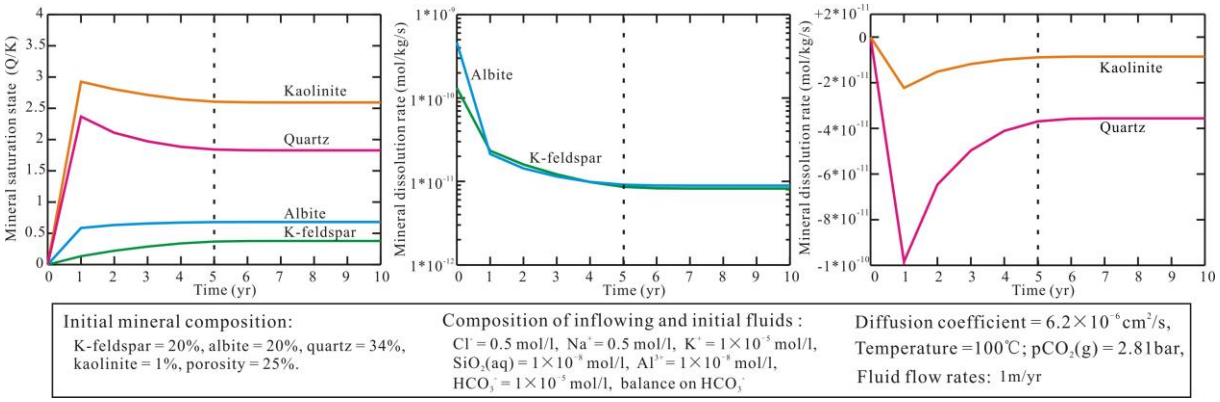

Figure 5. Ten years' evolution of mineral saturation and mineral reaction rates at the central part (X=5.0m, Y=1.05m) of the homogeneous geochemical system.

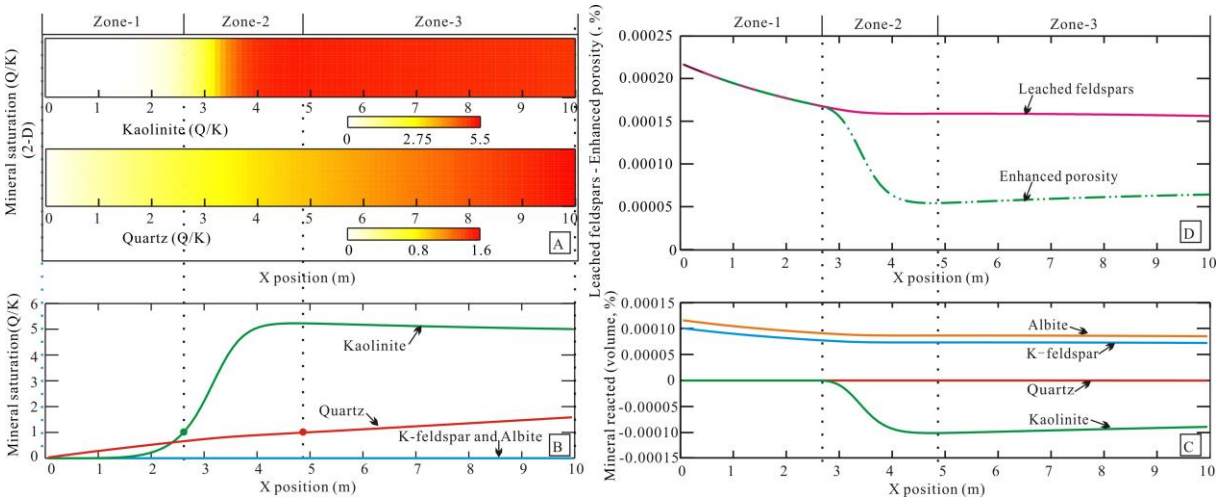

Figure 6. Zonation of modelling system at the 10th year of the simulation in the homogeneous system with temperature of 25℃ and flow rate of 10m/yr. A: 2-D plots showing the saturation evolution of kaolinite and quartz in the system from upstream side to downstream side at the 10th year. B: 1-D plots showing the saturation evolution of kaolinite, quartz, albite and K-feldspar in the middle part of the system (Y=1.05m, same for all other 1-D plots) from upstream side to downstream side at the 10th year. C: the amount of leached feldspars and porosity enhancement in different zones in the whole 10th year, the same with other figures; D: the amount of leached K-feldspar and albite and precipitated kaolinite and quartz in different zones in the whole 10th year, the positive values represent dissolution and negative values represent precipitation, the same with other figures. Detailed constraints of this simulation are given in figure 7. Zone-1: dissolution zone; Zone-2: transitional zone; Zone-3: precipitation zone.

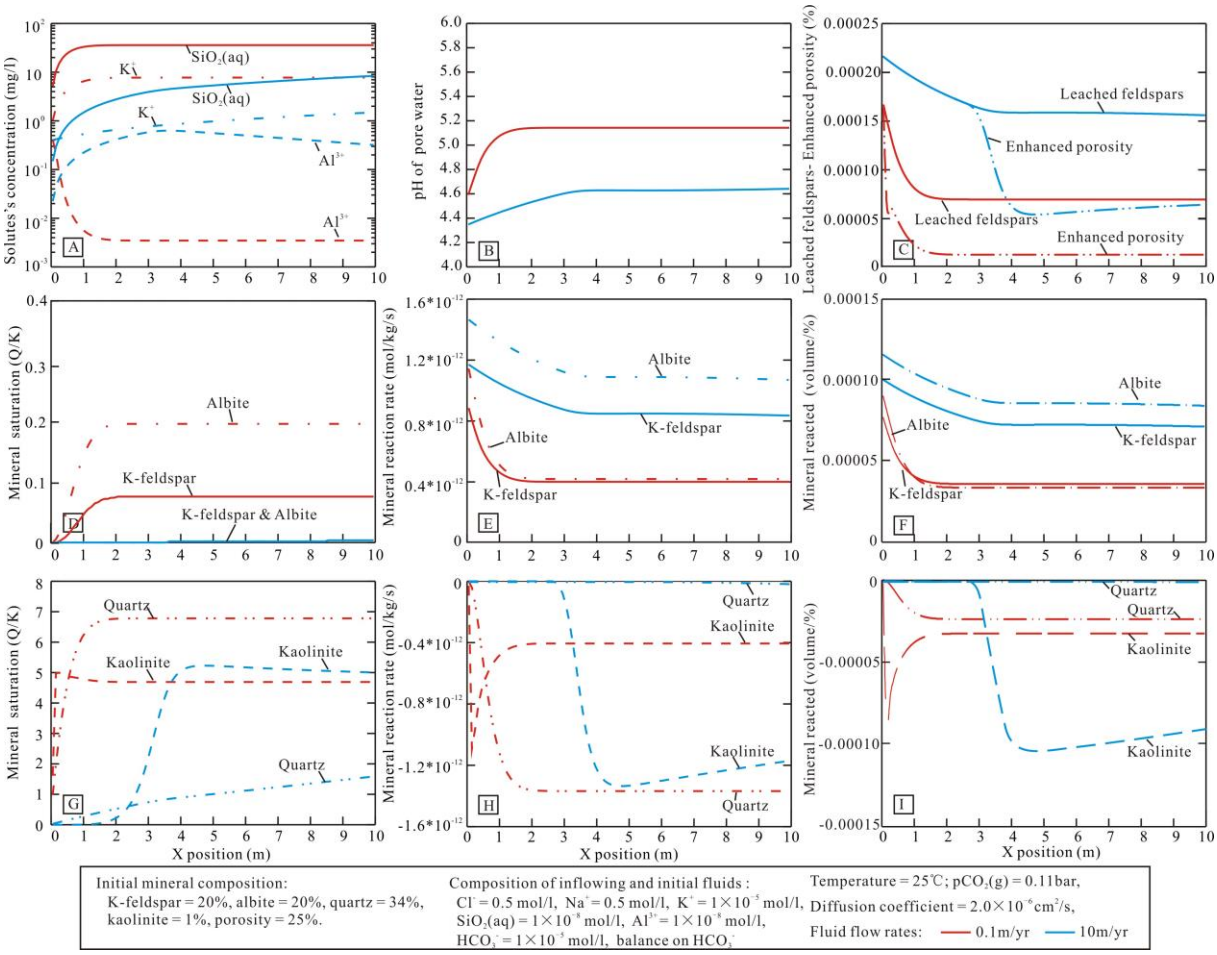

Figure 7. Results of simulations at 25℃ with the same reaction rate and inflowing fluid but different fluid flow rates of 0.1m/yr and 10m/yr.

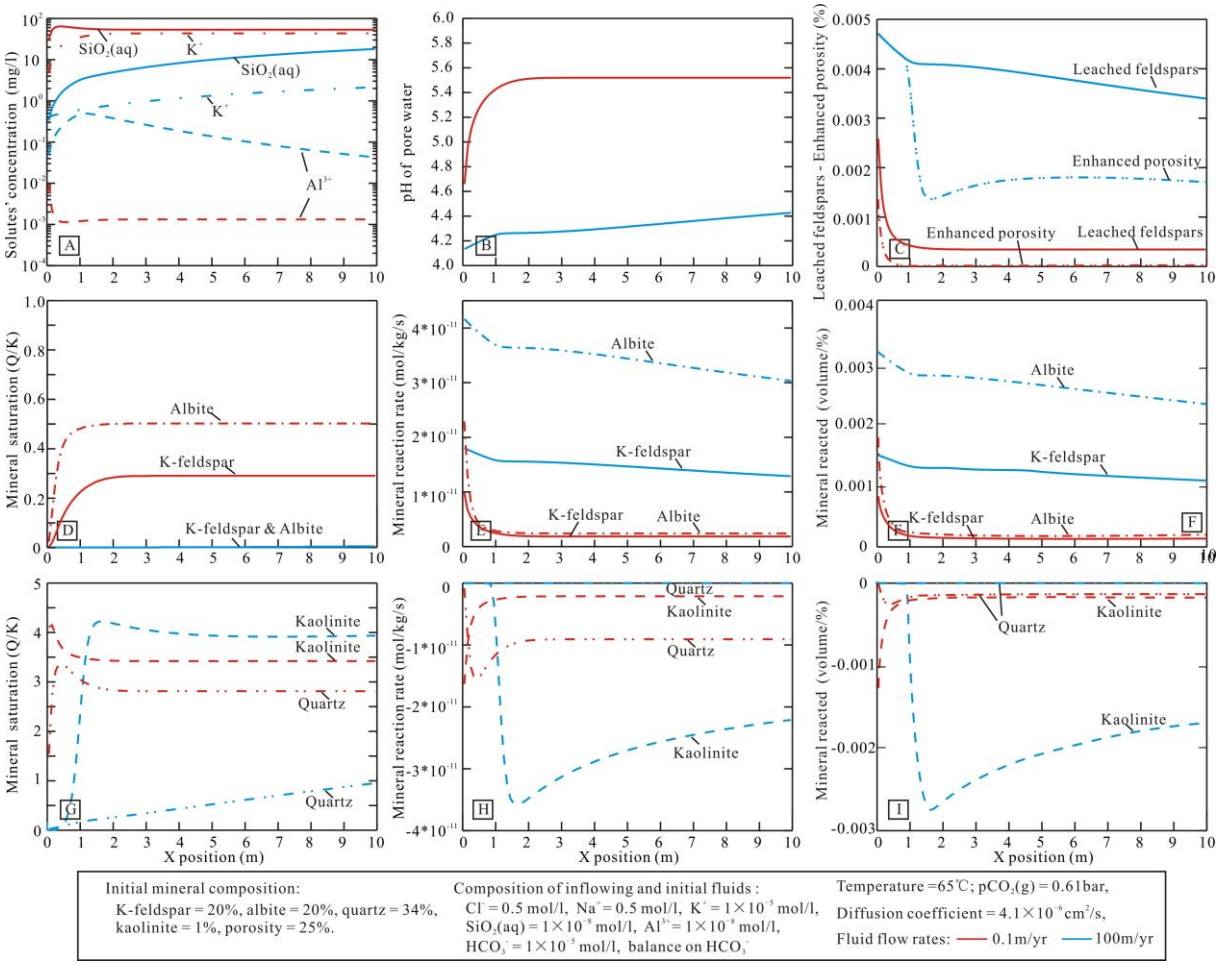

Figure 8. Results of simulations at 65℃ with the same reaction rate and inflowing fluid but different fluid flow rates of 0.1m/yr and 100m/yr.

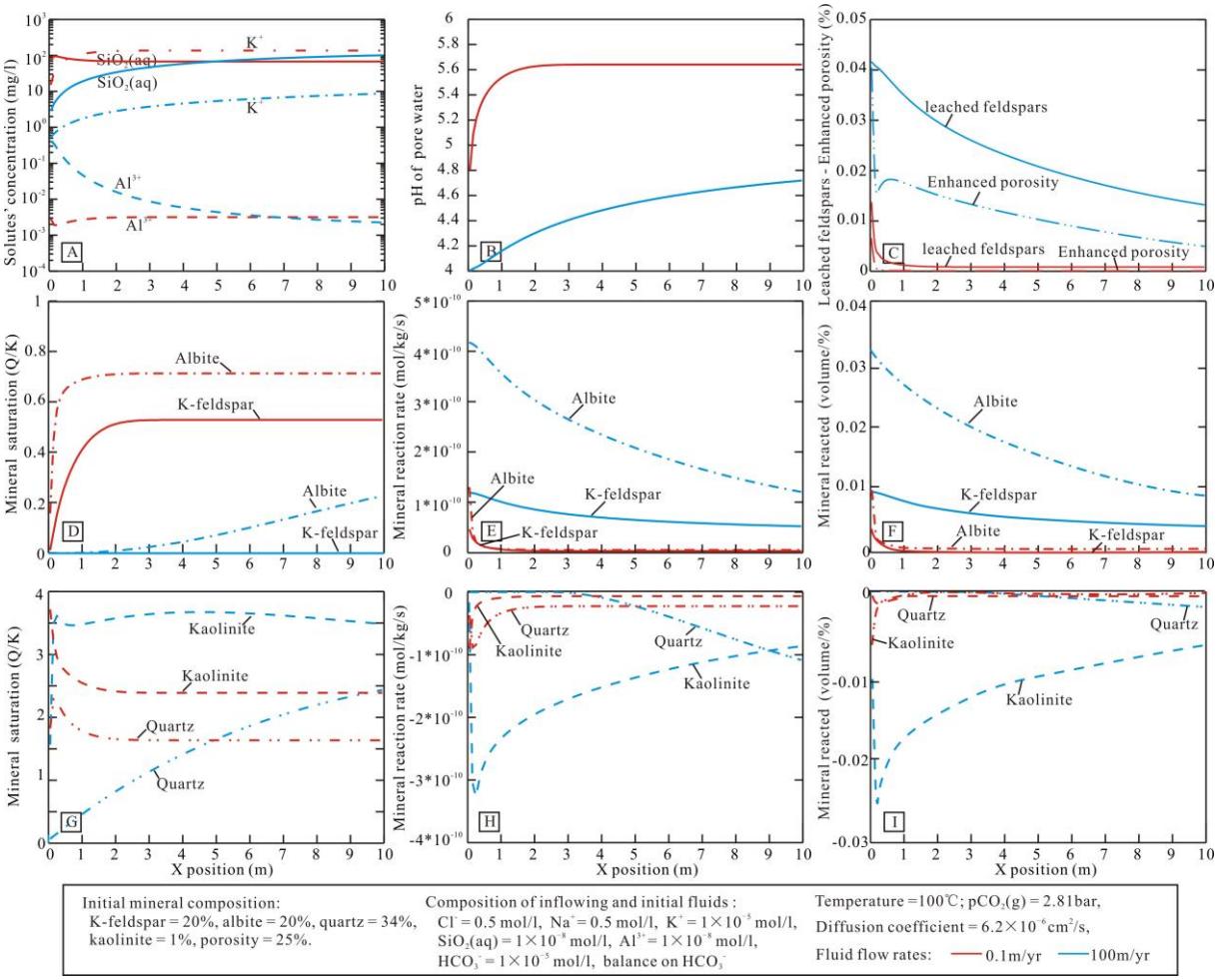

Figure 9. Results of simulations at 100℃ with the same reaction rate and inflowing fluid but different fluid flow rates of 0.1m/yr and 100m/yr.

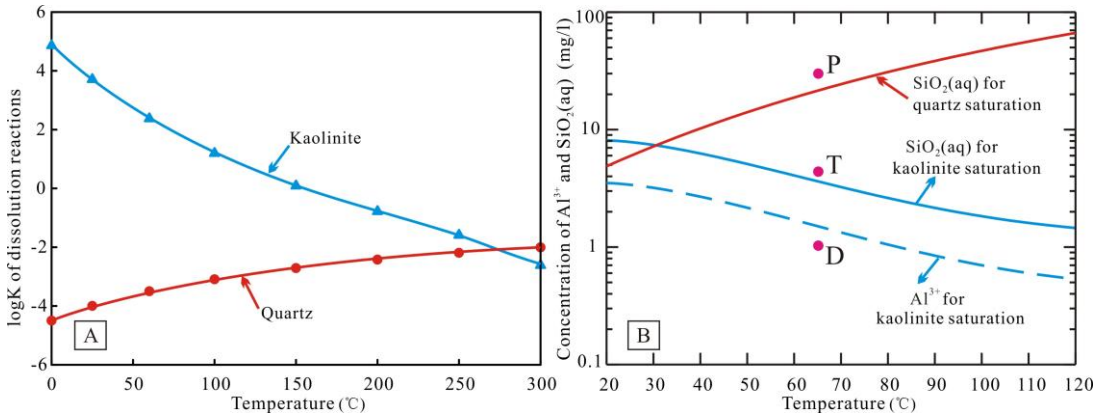

Figure 10. A-Log values of equilibrium constants of reverse reactions of Reaction-3 represented by Eq.(3) and Reaction-4 represented by Eq.(4). B-Concentrations of SiO_2(aq) and Al^{3+} needed for saturation of quartz and kaolinite at different temperature, based on GWB calculation. Point-P represents a fluid that is oversaturated with respect to both quartz and kaolinite, Point-T represents a fluid that is undersaturated with respect to quartz but oversaturated to kaolinite, and Point-D represents a fluid that is undersaturated with respect to both quartz and kaolinite,

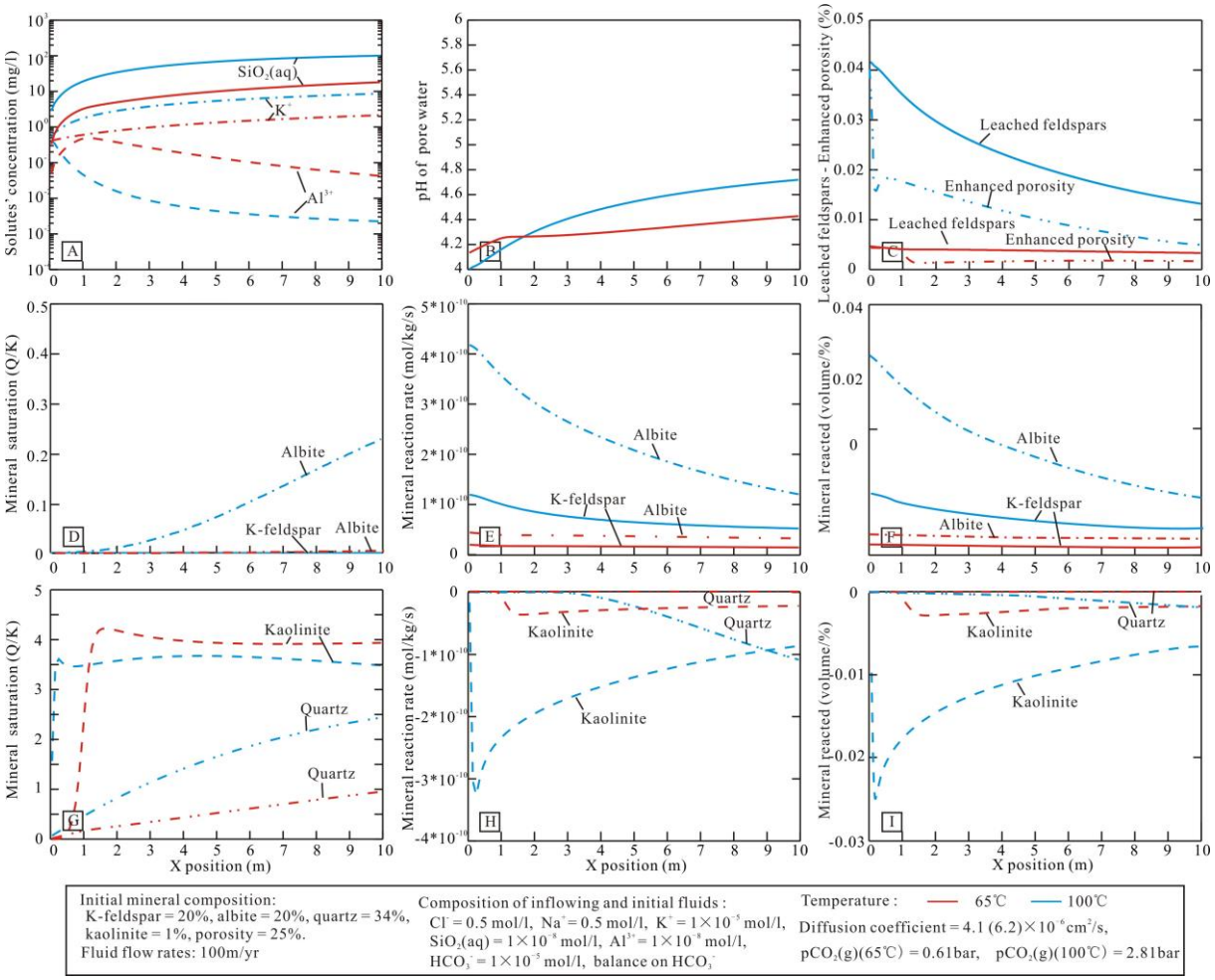

Figure11. Results of simulations at 65℃ and 100℃ with the same reaction rate, fluid flow rate and inflowing fluid.

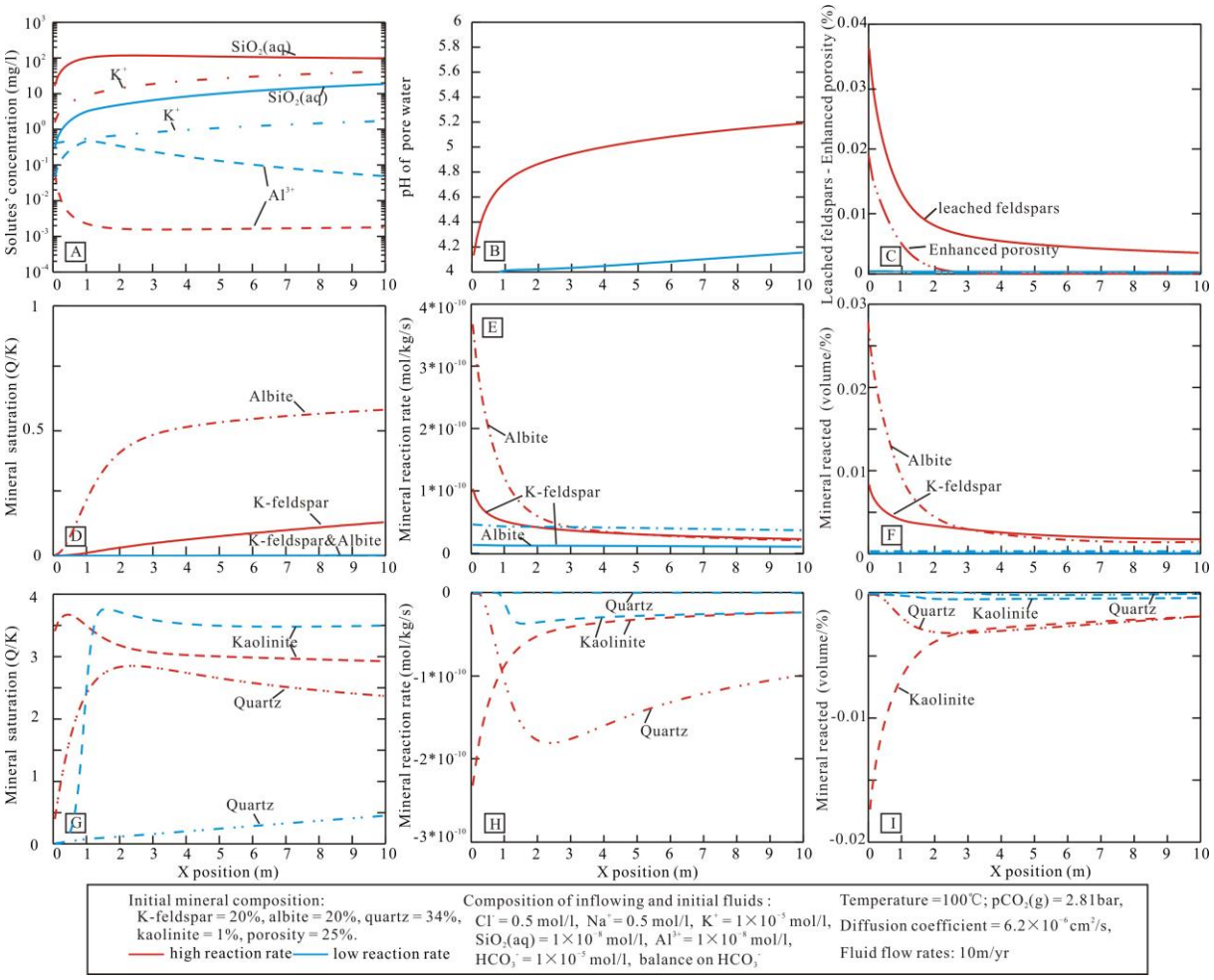

Figure 12. Results of simulations at 100℃ with the same inflowing fluid and flow rate but different reaction rates.

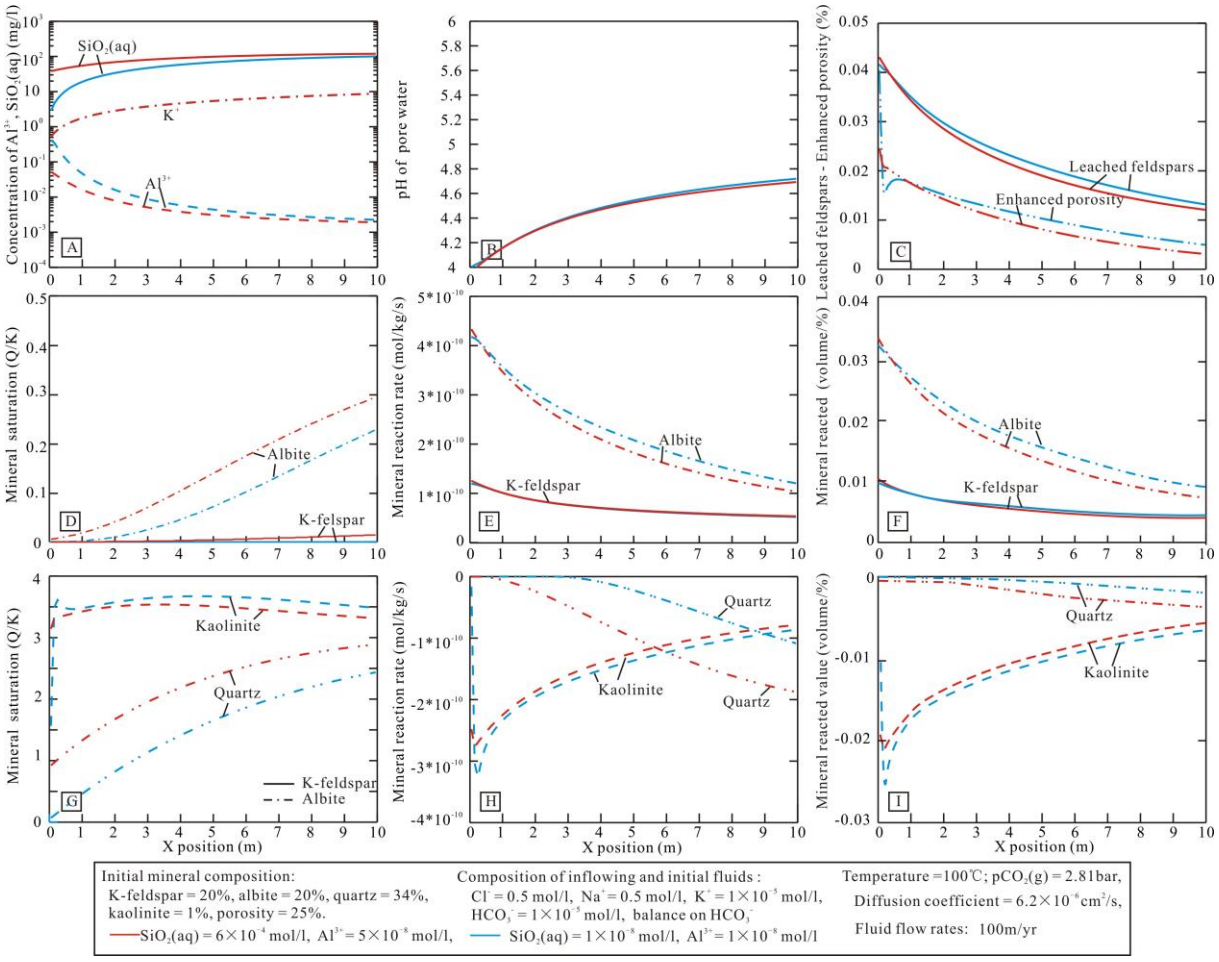

Figure 13. Results of simulations at 100℃ with the same reaction rate and fluid flow rate but inflowing fluids of different concentration of SiO_2(aq) and Al^{3+}.

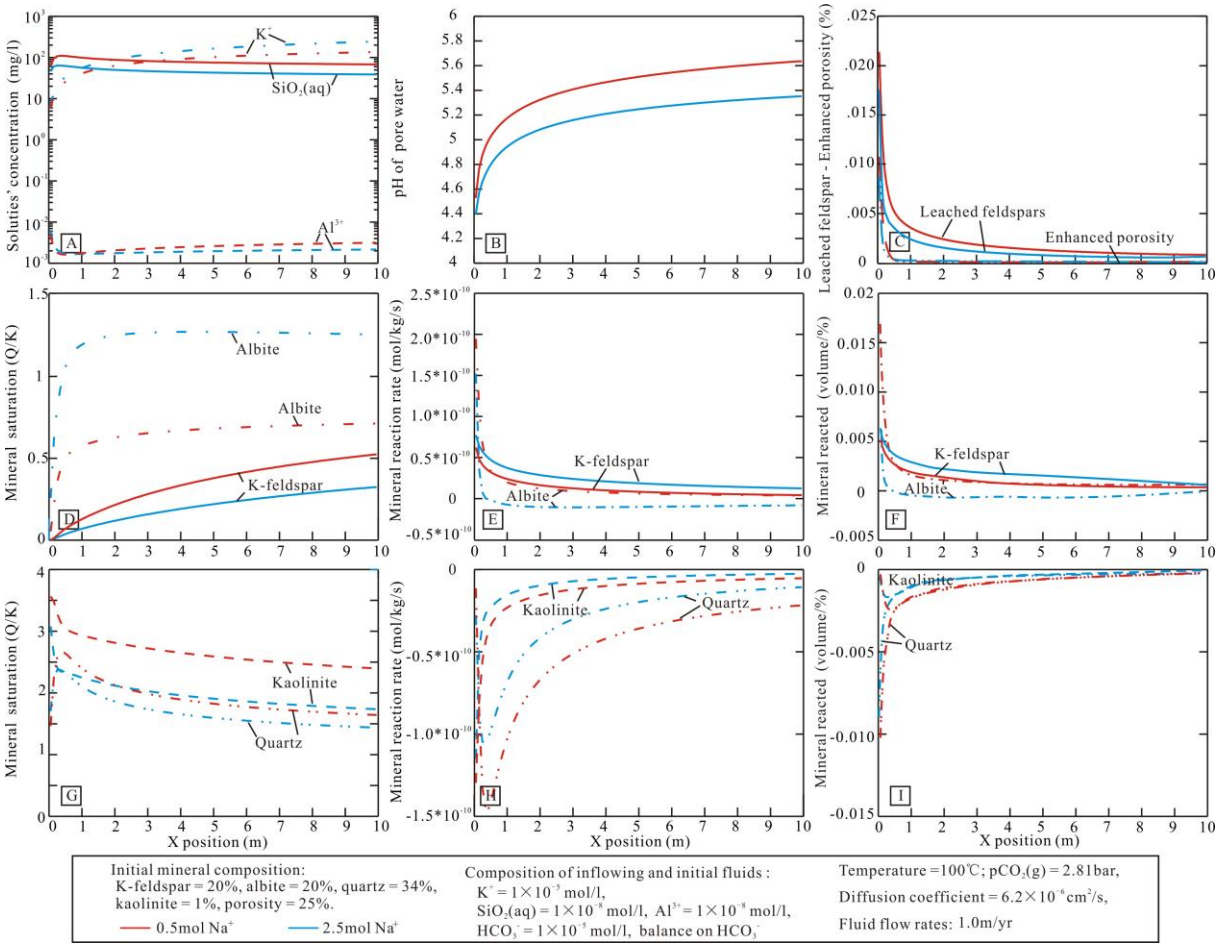

Figure 14. The 10th year results of simulations at 100℃ with the same reaction rate and fluid flow rate but inflowing fluids of different Na^+ concentration.

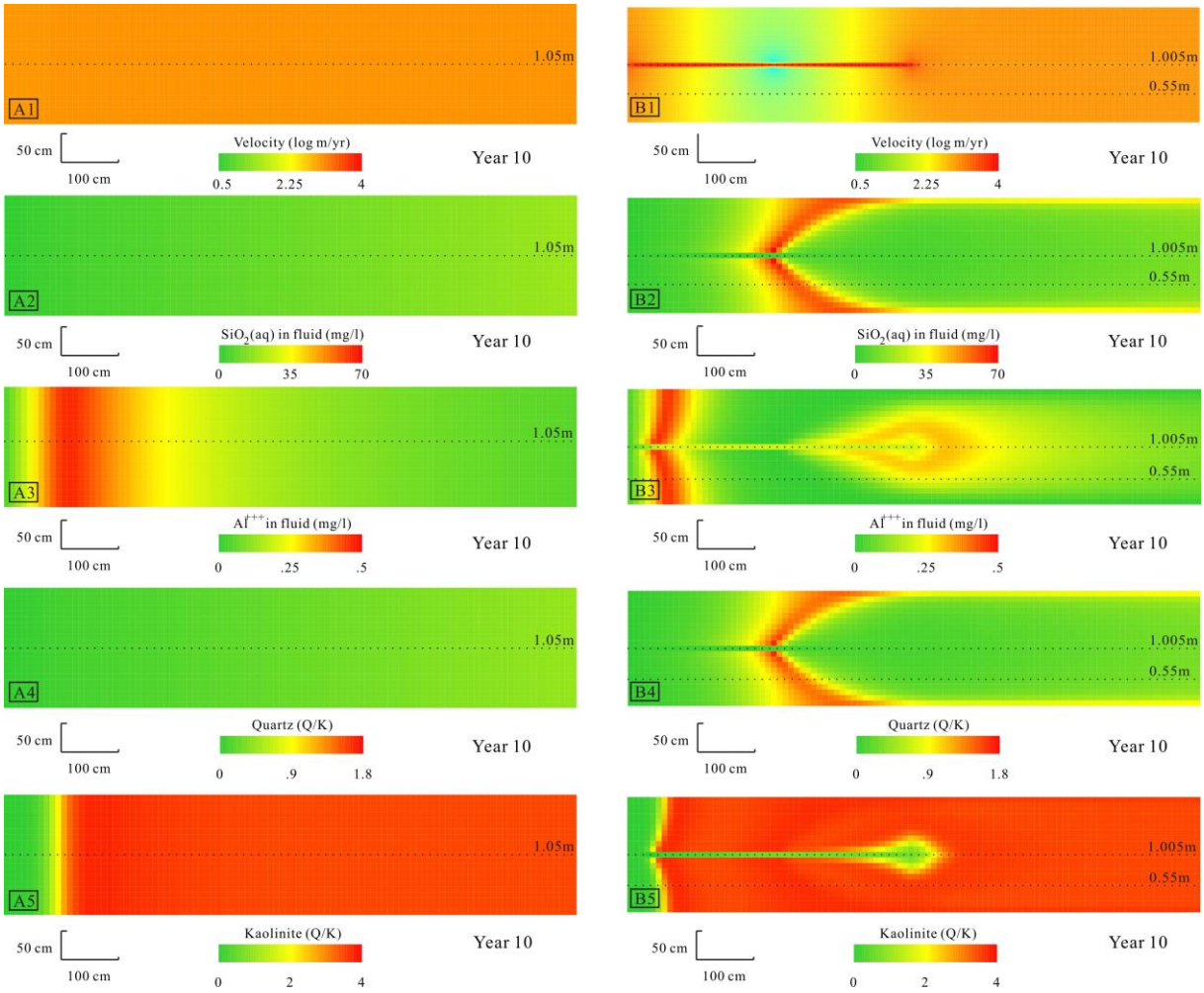

Figure 15. Results of simulationss at 100℃, with the same reaction rate, inflowing fluid and flow rate. Plots A1-A5 were results in the homogeneous modelling system without fracture, and plots B1-B5 were results in the modelling system with a fracture at the left side of the system. Values of different parameters at positions of black dashed lines in these two simulated systems were presented in Appendix figure 11.

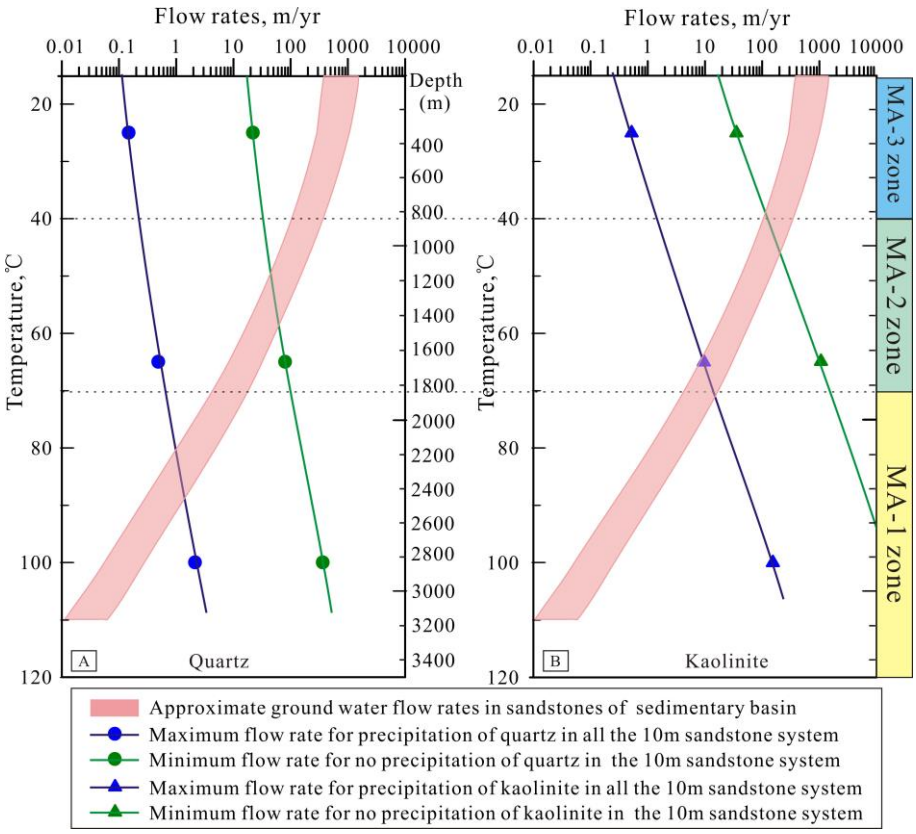

Figure 16. Temperature and flow rate sensitivity to transfer of SiO_2(aq) and Al^{3+} and secondary mineral precipitation. The maximum flow rate needed for precipitation of quartz and kaolinite in the whole sandstone system and the minimum flow rate needed for no precipitation of secondary minerals in the sandstone system were determined through simulations with reaction rates constrained by values in table 2. The approximate range of flow rates in sandstones of sedimentary basin were modified from Giles (1987). Simulations indicate that in a sedimentary basin without widely developed faults and fractures, MA-3, MA-2, and MA-1 probably occur in shallow, moderately, and deeply buried sandstone systems, respectively.

Table 1. Compositions of different solutes (mol/L) of initial pore water and inflowing fluids utilized in the simulations (HCO_3^- was balanced in simulations).

Ions / Fluids	Cl^-	Na^+	K^+	HCO_3^-	Al^{3+}	SiO_2(aq)
Initial pore water and inflowing fluid-1	0.5	0.5	1×10^{-5}	1×10^{-5}	1×10^{-8}	1×10^{-8}
inflowing fluid-2	2.5	2.5	1×10^{-5}	1×10^{-5}	1×10^{-8}	1×10^{-8}
inflowing fluid-3	0.5	0.5	1×10^{-5}	1×10^{-5}	5×10^{-8}	1×10^{-3}
inflowing fluid-4	0.52	0.5	0.02	1×10^{-5}	1×10^{-8}	1×10^{-8}

Table 2. List of kinetic rate parameters used in the simulations. n - reaction order with respect to H^+.

Minerals	k_m(mol/cm^2/sec), 25°C,pH= 0	Ea (KJ/mol)	k_m(mol/cm^2/sec), 65°C, pH=0	k_m(mol/cm^2/sec), 100°C, pH=0	Surface area (cm^2/g)	Nucleus (cm^2/cm^3)	pH dependence of rate $(a_{H^+})^n$ (n value)	References
K-feldspar	8.70×10^{-15}	51.70	1.02×10^{-13}	5.76×10^{-13}	9.8	/	0.500	(Palandri and Kharaka, 2004; Gonnenthal and Spyoher, 2001; Xu et al., 2005)
Albite	6.92×10^{-15}	65.00	1.54×10^{-13}	1.34×10^{-12}	9.8	/	0.457	
Quartz	1.02×10^{-18}	87.60	6.69×10^{-17}	1.24×10^{-15}	9.8	40	–	
Kaolinite	4.90×10^{-16}	65.90	1.14×10^{-14}	1.02×10^{-13}	2.5×10^4	600	0.777	(Palandri and Kharaka, 2004; Xu et al., 2005; Yang and Steefel, 2008)

Table.3 Species diffusivity ($D\times10^{-5}$cm^2/s) properties of select solutes at different 0℃, 25℃, 65℃ and 100℃.

Species	H^+	OH^-	K^+	$Al(OH)_3$	Al^{3+}	HCO_3^-	SiO_2（aq)	CO_2(aq)
Tc	54.4	25.9	9.55	4.46	2.15	5.06	5	5.5
Tf	1.555	2.094	0.409	0.243	0.116	0.275	0.5	0.325
D_0, 0℃	5.61	2.56	0.986	0.446	0.236	0.506	0.5	0.55
D_0, 25℃	9.31	5.27	1.96	1.0535	0.559	1.18	1.75	1.3625
D_0, 65℃	16	9.7	3.6	2.0	0.969	2.3	3.8	2.7
D_0, 100℃	20.99	23.53	5.045	2.876	1.375	3.256	5.5	3.8

Temperature dependence is expressed by $D_0=1.0\times10^{-6}(Tc+Tf\times T)$ (cm^2/sec). The equation and coefficients Tc and Tf that are obtained by fitting the data to the linear equation, are from Boudreau (1996), Li Yuanhui (1974) and Park (2014).

Table.4 Diffusion coefficient (D_0), Pe, D_H/D_0, and dispersivity (α) in homogeneous sandstones with different temperatures and flow rates.

Sandstones	Flow rate, m/yr	Porosity,%	Grain size, cm	D_0, $1\times10^{-5}cm^2/s$	Pe	D_H/D_0	α, cm
25℃	0.01	25	0.05	1	0.000053	0.4	61.212
	0.1	25	0.05	1	0.000528	0.4	6.121
	1	25	0.05	1	0.005285	0.4	0.612
	10	25	0.05	1	0.052849	0.4	0.061
	100	25	0.05	1	0.528496	0.5	0.009
	1000	25	0.05	1	5.284965	2.5	0.002
65℃	0.01	25	0.05	2	0.0000264	0.4	122.425
	0.1	25	0.05	2	0.000264	0.4	12.242
	1	25	0.05	2	0.002642	0.4	1.224
	10	25	0.05	2	0.026425	0.4	0.122
	100	25	0.05	2	0.264248	0.4	0.012
	1000	25	0.05	2	2.642483	1.9	0.011
100℃	0.01	25	0.05	3	0.000017	0.4	183.636
	0.1	25	0.05	3	0.000176	0.4	18.363
	1	25	0.05	3	0.001762	0.4	1.836
	10	25	0.05	3	0.017616	0.4	0.183
	100	25	0.05	3	0.176165	0.4	0.018
	1000	25	0.05	3	1.7616551	1.4	0.011